Evaluating year-to-year anomalies in tropical wetland methane emissions using satellite CH$_4$ observations

Robert J. Parker[a,b,c,*], Hartmut Boesch[a,b,c], Joe McNorton[c,d], Edward Comyn-Platt[f], Manuel Gloor[e], Chris Wilson[c,d], Martyn P. Chipperfield[c,d], Garry D. Hayman[f], A. Anthony Bloom[g]

[a] Earth Observation Science, Department of Physics and Astronomy, University of Leicester, Leicester, UK
[b] Leicester Institute for Space and Earth Observation, University of Leicester, Leicester, UK
[c] NERC National Centre for Earth Observation, UK
[d] School of Earth and Environment, University of Leeds, UK
[e] School of Geography, University of Leeds, UK
[f] Centre for Ecology and Hydrology, Wallingford, UK
[g] Jet Propulsion Laboratory, California Institute of Technology, Pasadena, CA, USA

ARTICLE INFO

ABSTRACT

Natural wetlands are the largest source of methane emissions, contributing 20–40% of global emissions and dominating the inter-annual variability. Large uncertainties remain on their variability and response to climate change.

This study uses atmospheric methane observations from the GOSAT satellite to evaluate methane wetland emission estimates. We assess how well simulations reproduce the observed methane inter-annual variability by evaluating the detrended seasonal cycle. The latitudinal means agree well but maximum differences in the tropics of 28.1–34.8 ppb suggest that all simulations fail to capture the extent of the tropical wetland seasonal cycle.

We focus further analysis on the major natural wetlands in South America: the seasonally flooded savannah of the Pantanal (Brazil) and Llanos de Moxos (Bolivia) regions; and the riverine wetlands formed by the Paraná River (Argentina). We see large discrepancies between simulation and observation over the Pantanal and Llanos de Moxos region in 2010, 2011 and 2014 and over the Paraná River region in 2010 and 2014. We find highly consistent behaviour between the time and location of these methane anomalies and the change in wetland extent, driven by precipitation related to El Niño Southern Oscillation activity.

We conclude that the inability of land surface models to increase wetland extent through overbank inundation is the primary cause of these observed discrepancies and can lead to under-estimation of methane fluxes by as much as 50% (5.3–11.8 Tg yr^{-1}) of the observed emissions for the combined Pantanal and Paraná regions. As the hydrology of these regions is heavily linked to ENSO variability, being able to reproduce changes in wetland behaviour is important for successfully predicting their methane emissions.

1. Introduction

Methane (CH$_4$) is an important greenhouse gas, contributing ~30% of the radiative forcing due to anthropogenic long-lived greenhouse gases released to the atmosphere since the industrial revolution. It is second only to carbon dioxide (CO$_2$) and has a global warming potential on a 100-year time-scale of over 25 times that of CO$_2$ (Etminan et al., 2016). Global atmospheric concentrations of CH$_4$ are now approximately 1810 parts per billion (ppb), an increase of over 1000 ppb from pre-industrial levels (Myhre et al., 2013). However, neither the causes of recent inter-decadal variability in the global atmospheric growth rate

nor if the current growth will continue are fully understood. Surface observations from a range of networks (NOAA, AGAGE, CSIRO and UCI) have shown that the growth rate of atmospheric CH$_4$ had been steadily declining over the last three decades, from 12 ppb yr^{-1} in the 1980s, to 6 ppb yr^{-1} in the 1990s to almost no growth in the early 2000s (Dlugokencky et al., 2003; Kirschke et al., 2013). The apparent stabilisation of atmospheric CH$_4$ suggested an equilibrium between the various sources and sinks. However, the sudden and unexpected renewed growth from 2007 has highlighted significant gaps in current knowledge (Rigby et al., 2008; Dlugokencky et al., 2009; Nisbet et al., 2014) with various hypotheses presented to explain the behaviour

---

(Nisbet et al., 2016; Schaefer et al., 2016; McNorton et al., 2016a; Rigby et al., 2017; Turner et al., 2017).

The main sources of atmospheric CH_4 are natural wetlands, rice cultivation, fossil fuel production, livestock and biomass burning (Saunois et al., 2016). Wetland emissions contribute between 20–40% of the total global CH_4 emissions (Ciais et al., 2013). They are thought to dominate the inter-annual variability of global CH_4 (Bousquet et al., 2006) but there remain large uncertainties surrounding their variability and potential response to climate change. This uncertainty is dominated by estimates of wetland extent and distribution (Bloom et al., 2010; Melton et al., 2013; Kirschke et al., 2013). Furthermore, the extent and distribution of wetlands and the rate of methanogenesis are sensitive to changing climate, leading to a potential positive feedback on climate (Christensen et al., 2003; Gedney et al., 2004).

The majority of natural wetlands are found in tropical and subtropical regions where precipitation drives the variability in wetland extent, and ultimately CH_4 emissions (Bloom et al., 2010). Tropical precipitation is strongly enhanced during the La Niña phase of the El Niño Southern Oscillation (ENSO) and previous work has attributed higher tropical wetland CH_4 emissions to this (Hodson et al., 2011; Zhu et al., 2017). Bousquet et al. (2006) and Ringeval et al. (2010) suggest that it is these tropical wetlands that drive the majority of the year-to-year variability in atmospheric CH_4 and have a significant impact on the global CH_4 budget (Hodson et al., 2011). However, there remain substantial data gaps and discrepancies between process-based estimates and those from atmospheric inversions (Bousquet et al., 2011; Melton et al., 2013). Improvements to process-based modelling of wetland extent and subsequent wetland CH_4 emissions are identified by Saunois et al. (2016) as a key priority for improving our understanding of the global CH_4 budget.

This work aims to i) evaluate the temporal and spatial global variability of state-of-the-art CH_4 emission datasets against satellite observations; ii) test our current capability to accurately reproduce the observed tropical CH_4 seasonal cycle over major wetland regions; and iii) estimate the discrepancy in emissions between models and observations over these regions.

2. CH_4 wetland emission estimates

There have been many previous studies assessing how well wetland CH_4 emissions can be reproduced by current land surface models (LSMs), often finding large uncertainties in both the spatial and temporal distribution (Riley et al., 2011; Melton et al., 2013; Kirschke et al., 2013). When such emission estimates are used as prior estimates in forward model experiments or atmospheric transport inversions for CH_4 flux estimates they are not fully consistent with in-situ or satellite CH_4 observations (Fraser et al., 2013; Hayman et al., 2014).

In this work we use four different CH_4 wetland emission estimates, from both top-down and bottom up approaches. A comparison (Fig. 1) reveals that these emission estimates can vary considerably from each other in regions with major wetlands.

2.1. JULES - land surface model methane emission estimates

We use two emission estimates based on The Joint UK Land Environment Simulator (JULES; Best et al. (2011), Clark et al. (2011)). JULES is a process-based land surface model (LSM) that describes the exchange of water, energy and carbon between the land surface and atmosphere. JULES monthly methane wetland emission estimates at a spatial resolution of 0.5° provided by both University of Leeds (McNorton et al. (2016b); referred to as JULES-Leeds from here on) and the Centre for Ecology and Hydrology (CEH) (Comyn-Platt et al. (2018,

Gedney et al. (in preparation); referred to as JULES-CEH from here on) are used. Further details for the two JULES-based estimates are provided in Appendix A.

2.2. Bloom2012 - top-down wetland methane emission estimates

Bloom et al. (2010, 2012) used a diagnostic modelling approach, further constrained by satellite-derived CH_4 concentration variability, to estimate CH_4 wetland fluxes. They combine equivalent water height anomalies from GRACE (Landerer and Swenson, 2012) and ERA-interim surface skin temperature in a diagnostic wetland emission model; the model seasonality is empirically constrained by atmospheric total column CH_4 variability estimated from space by SCIAMACHY. Water table depth is determined to be the main contributor to variations in the observed CH_4 in the tropical regions, with the land surface temperature playing a more important role at higher latitudes. These Bloom2012 emission estimates have been used by many CH_4 inversion studies as an a priori estimate of methane wetland emissions (Bloom et al., 2012; Fraser et al., 2011, 2013; Wilson et al., 2014). Studies have shown that use of these wetland emission estimates, together with emissions from fossil fuels and biomass burning within atmospheric transport models as surface boundary conditions are generally able to sufficiently reproduce atmospheric CH_4 observations.

2.3. WetCHARTs - process-based data-constrained wetland methane emissions

Bloom et al. (2017) derive a wetland CH_4 emission and uncertainty datasets from an ensemble of terrestrial biosphere models (Huntzinger et al., 2013), a terrestrial carbon cycle analysis (Bloom et al., 2016), satellite-derived surface water extent (Schroeder et al., 2015), ERA-interim reanalyses, and wetland extent maps (Lehner and Döll, 2004; Bontemps et al., 2011). The WetCHARTs emission estimates are constrained by the extent of wetlands as defined in the Global Lakes and Wetlands Database (Lehner and Döll, 2004), and the GLOBCOVER wetland extent dataset (Bontemps et al., 2011). These emission estimates cover a period of 2001 to 2015. A nominal benefit of this approach is that the combination of satellite data with carbon cycle models and temperature-based parametrisations leads to physical-based estimates of the uncertainty, which can be used to characterise uncertainties of atmospheric transport inversions for the purpose of CH_4 flux estimation.

3. GOSAT proxy XCH_4 data

We use observations of column-averaged dry air mole fractions of CH_4 (XCH_4) from the University of Leicester Proxy XCH_4 GOSAT retrieval (v7). Details of these data are available in Parker et al. (2011, 2015). In short, the retrieval uses the University of Leicester retrieval algorithm (Boesch et al., 2011; O'Dell et al., 2012) to retrieve XCH_4 using the light-path proxy approach (Frankenberg et al., 2006) from GOSAT shortwave infrared radiances (Parker et al., 2011). This proxy approach is particularly useful over regions such as the tropics where the prevalence of clouds and aerosols can greatly reduce the number of successful "full physics" retrievals. Many recent inversion studies (Fraser et al., 2013; Wecht et al., 2014; Fraser et al., 2014; Cressot et al., 2014; Wilson et al., 2014; Alexe et al., 2015; Turner et al., 2015) have used the University of Leicester Proxy XCH_4 data in order to successfully infer regional and global emissions.

This GOSAT XCH_4 data has been extensively validated (Dils et al., 2014; Parker et al., 2015; Buchwitz et al., 2017), primarily using data from the Total Carbon Column Observing Network (TCCON). TCCON is
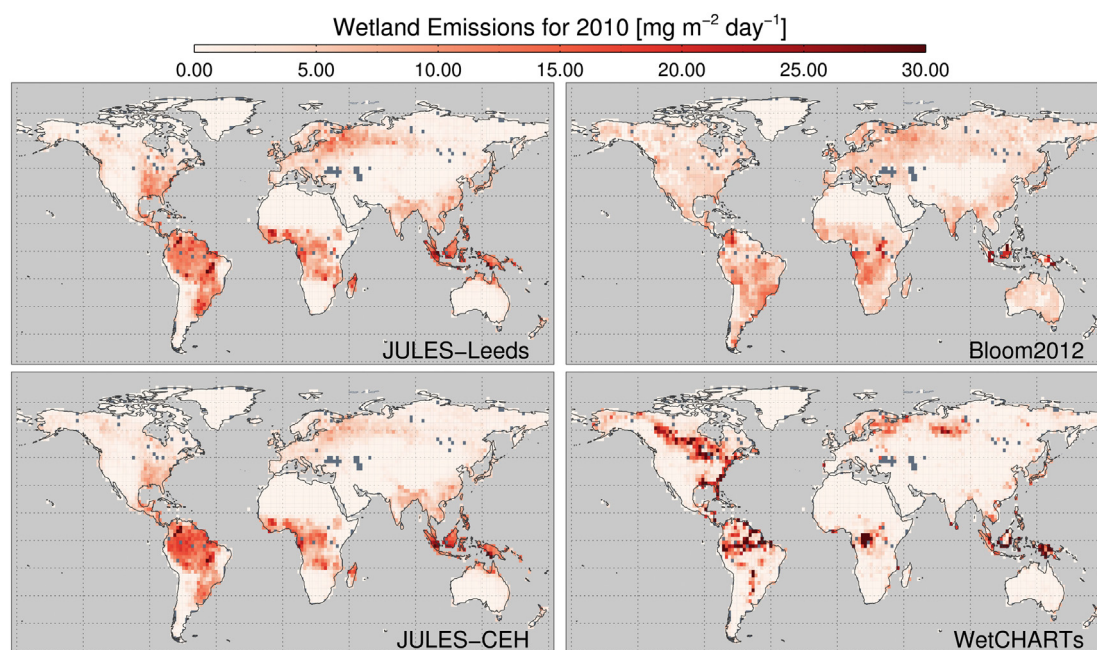
Fig. 1. Global maps showing the CH$_4$ wetland emission data for 2010 from the four different estimates used in this study.

a global network of ground-based high resolution Fourier transform spectrometers recording direct solar spectra in the near-infrared spectral region (Wunch et al., 2011b). The TCCON data are calibrated to World Meteorological Organization (WMO) standards (Wunch et al., 2010) and are the primary validation data for satellite observations of greenhouse gases (Cogan et al., 2012; Wunch et al., 2011a; Dils et al., 2014).

Version 7 of our GOSAT Proxy XCH$_4$ data has been assessed against the latest version (GGG2014) of the TCCON data. Across all sites, the standard deviation of the 44,714 individual co-located pairs (i.e. the single-sounding precision) is found to be just 13.28 ppb with a correlation coefficient of 0.89 and overall bias of just 0.06 ppb. The TCCON network is limited in its geographic distribution with the majority of sites measuring in the northern hemisphere (US, Europe and Japan). Although TCCON measurements in the tropics are limited, the data which are available agree well with GOSAT (Paramaribo bias of 3.4 ppb, Ascension Island bias of 3.1 ppb).

To further validate GOSAT over the Amazon, Webb et al. (2016) used high-precision in-situ aircraft measurements from the AMAZON-ICA and Amazonian Carbon Observatory projects (Webb et al., 2016). They found that GOSAT XCH$_4$ and the aircraft measurements agree within their uncertainties and that the GOSAT data successfully capture the phase and magnitude of the seasonal cycle over the Amazon (r = 0.61–0.90).

Overall, these validation efforts suggest that the GOSAT Proxy XCH$_4$ data are of sufficient accuracy and precision to successfully assess the seasonal cycle of CH$_4$ driven by wetland emissions.

4. Modelling of atmospheric CH$_4$

We use the TOMCAT atmospheric chemistry transport model (University of Leeds - (Chipperfield, 2006)) to simulate atmospheric CH$_4$ concentrations with prescribed surface emission fields. We perform simulations between 2009 and 2014 at 2.8° × 2.8° spatial resolution with 60 vertical levels for each wetland emission dataset described in Section 2. All other CH$_4$ flux components are kept the same. We use the

EDGAR anthropogenic emissions up to 2010 (Olivier et al., 2012), with extrapolated values for the latter years, and take biomass burning emissions from GFEDv4.1 (Randerson et al., 2015). For CH$_4$ sources with limited inter-annual variability (termites, oceans and hydrates) we use annually repeated values as described in Patra et al. (2011). For emissions from rice paddies that reside in natural wetland areas, in order to consistently evaluate all wetland datasets we prescribe annual repeated values for the rice production (Yan et al., 2009). Loss fields are as used in McNorton et al. (2016a), with annually repeating OH and stratospheric O^{1}D loss fields and a methanotrophic soil sink.

Assumptions made relating to the distribution of the OH sink, as well as transport and other non-wetland emissions are all factors that could contribute to uncertainties in the analysis. The scale of OH uncertainty could be investigated by performing sensitivity experiments using multiple OH fields; this is beyond the scope of this study. However, as the uncertainty in OH distribution would cause discrepancies at a much larger regional scale than we observe in our analysis, we remain confident that wetland emissions are the dominant effect that we observe.

5. Detrending the CH$_4$ seasonal cycle

To asses the magnitude and phase of the wetland seasonal cycle we detrend the modelled and observed atmospheric CH$_4$ so that any inconsistencies between the trends from GOSAT and the simulations (e.g. due to interpolation of the anthropogenic emissions in latter years or assumptions about variations of the OH sink) are minimised. We detrend the GOSAT XCH$_4$ data and model simulations using the NOAA CurveFit routine (Thoning et al., 1989). This performs a least squares fit of a third order polynomial to account for the long-term growth with the annual oscillation relating to the seasonal cycle fit through a series of harmonics. The uncertainty on the detrended seasonal cycle is derived from the sum of the standard deviations of the smoothed component and the trend of the fitted data (NOAA, 2017).

Fig. 2 shows a comparison of the detrended TCCON and GOSAT seasonal cycles for the US sites at Park Falls (45.945°N, 90.273°W -
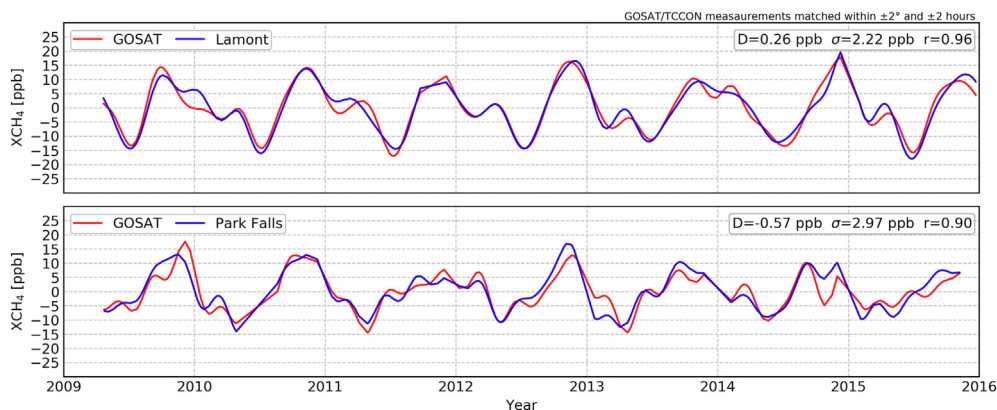
Fig. 2. Comparison of the smoothed detrended TCCON XCH$_4$ seasonal cycle at the US Lamont and Park Falls TCCON sites against GOSAT XCH$_4$ observations within ±2° latitude/longitude and ±2 h. The average difference (D), standard deviation of the difference (σ) and correlation coefficient (r) between the datasets are all shown.

Wennberg et al. (2014a)) and Lamont (36.604°N, 97.486°W - Wennberg et al. (2014b)). We find average differences ≤0.6 ppb, standard deviations below 3 ppb and high correlation coefficients (0.90–0.96). The close agreement between GOSAT and TCCON data gives confidence that the methodology used is suited to estimate the XCH$_4$ seasonal cycle.

6. Global comparisons

We assess how well the global distribution of the observed CH$_4$ seasonal cycle can be reproduced by the emission estimates. To allow a robust comparison between the models and the satellite data, the models are sampled at the same time and location as the GOSAT observations and have the measurement-specific GOSAT averaging kernel applied.

The difference in the global daily average zonal mean values between model and observation are found to be small for all model simulations. The average differences (±standard deviations) were 2.2 ± 7.0 ppb (JULES-Leeds), 1.7 ± 6.9 ppb (JULES-CEH), 2.7 ± 8.0 ppb (Bloom2012) and 2.5 ± 8.1 ppb (WetCHARTs). However, there is clear spatial structure in the differences to observations (see Appendix B). The largest differences were at tropical latitudes where the models generally under-estimated w.r.t. GOSAT. We attribute this difference to underestimation of tropical (particularly South American) wetland emissions in all of these model simulations.

The regions of notable model/satellite differences are known wetland regions, suggesting that these differences are related to wetland

fluxes. Uncertainties in OH concentration would occur over non-wetland regions as well as wetland regions leading to a different spatial and temporal distribution of model/satellite discrepancy. The scale of OH uncertainty could be investigated by performing sensitivity experiments using multiple OH fields; this is beyond the scope of this study.

7. Regional analysis

We identify individual regions of interest which are dominated by natural wetland emissions (Fig. 3) using the Sustainable Wetlands Adaptation and Mitigation Program (SWAMP) data from the Center for International Forestry Research (CIFOR) (Gumbricht et al., 2017). This compilation identifies all major wetlands between 60°S and 40°N. Although there is no temporal component, the data can be used to identify regions where we would expect a significant wetland extent and subsequently large CH$_4$ emissions.

We calculate the CH$_4$ seasonal cycle for each region and the contribution of each component (i.e. wetlands, biomass burning, anthropogenic, rice paddies) to the overall seasonal cycle amplitude. Fig. 4 shows the peak-to-peak wetland seasonal cycle for GOSAT and the model simulations. The fire, rice and anthropogenic seasonal cycle magnitudes are also displayed. Note that the GOSAT wetland seasonal cycle magnitude assumes that the difference between the GOSAT observations and the NoWetlands simulation can be fully attributed to differences in wetland emissions.

We find that for wetland regions located in Asia, where rice production and anthropogenic emissions can both be significant, the
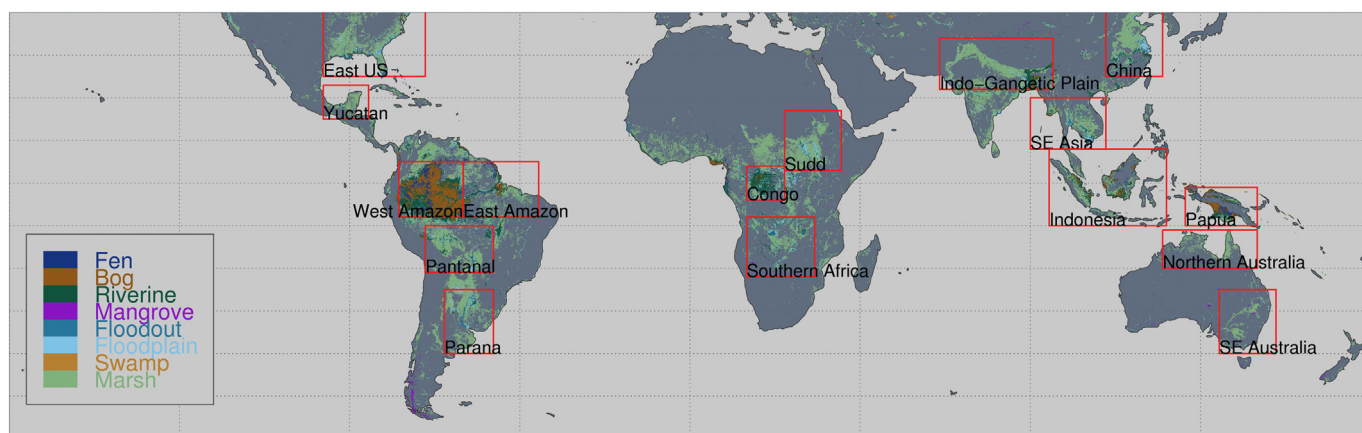

Fig. 3. Map showing the location of the individual wetland regions identified using the Sustainable Wetlands Adaptation and Mitigation Program (SWAMP) data from the Center for International Forestry Research (CIFOR).
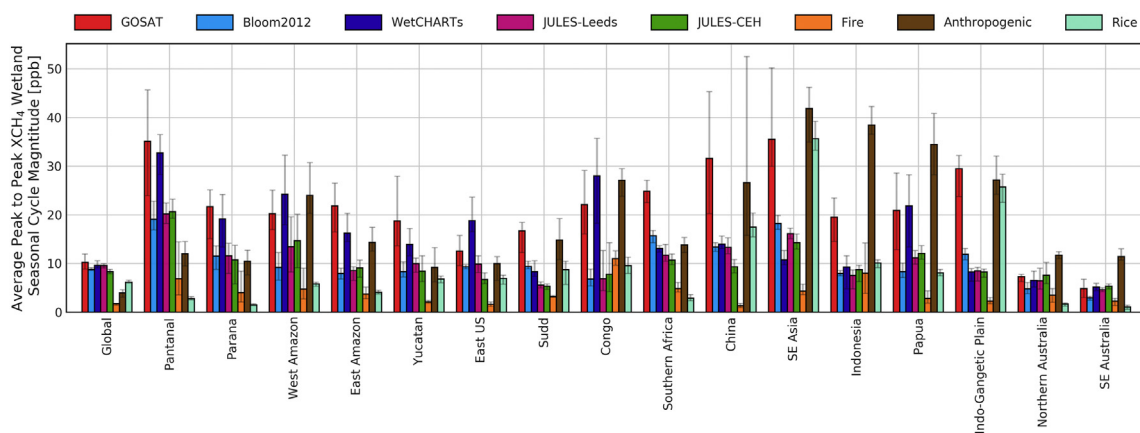
Fig. 4. Magnitude of the average (2010–2014) peak-to-peak wetland CH$_4$ seasonal cycle globally and in each of the 16 regions of interest as identified in Fig. 3. The wetland component of the seasonal cycle is calculated by subtracting the model simulation containing no wetland emissions from each of the full model simulations and from the GOSAT data. The individual components for fire, rice and anthropogenic emissions are calculated from the model data in the same way (and are identical for all four model simulations). The error bars indicate the min/max annual values.

observed total seasonal cycle is at its largest (peaking at 84.69 ± 4.63 ppb in SE Asia in 2012) but is exceeded by all of the model simulations (by 11.8–16.25 ppb). This discrepancy is attributed to the uncertainty in the anthropogenic and rice emissions in this region which dominate the wetland signal and is consistent with previous studies which have suggested that estimates of these non-wetland emissions over Asia are too high (Patra et al., 2009; Hayman et al., 2014).

The Pantanal, Paraná, Yucatán and Southern African regions all exhibit strong seasonal cycles in CH$_4$ that are dominated by wetland emissions. The Pantanal and Paraná regions are examined in detail in the following sections, particularly in relation to how well JULES is capable of reproducing the observed atmospheric concentration signals. The Yucatán and Southern African regions are examined in Appendix D and provide corroboration of the results for South America.

7.1. Pantanal

The Pantanal wetland region is the world's largest tropical wetland complex and extends over parts of Brazil, Bolivia and Paraguay with an area estimated at around 160,000 km^2 (Junk and de Cunha, 2005). For this analysis we also include the large Bolivian seasonally inundated savannah (Llanos de Moxos) located to the north-west, defining our "Pantanal" region from 70°W to 52°W and 21°S to 10°S.

Fig. 5 (top panel) shows the detrended seasonal cycles for this region. All datasets exhibit a strong seasonal cycle, with average amplitudes of 35.11 ± 2.62 ppb (GOSAT), 26.31 ± 2.77(JULES-Leeds), 25.37 ± 2.83(JULES-CEH), 26.61 ± 2.44(Bloom2012) and 31.94 ±

3.04(WetCHARTs). The correlation coefficients range from 0.85 to 0.90 and the standard deviation of the model-GOSAT difference is less than 6 ppb. When omitting any wetland emissions from the simulation, the statistics worsen substantially, showing that the addition of the wetland datasets greatly improves the capability of the model to reproduce the observed seasonal cycle in this region.

Large discrepancies (~10–20 ppb) in the seasonal cycle magnitude between the observations and models are found for multiple (2010, 2011 and 2014) but not all years (2012 and 2013). This is consistent with Webb et al. (2016) who observed total column enhancements of over 50 ppb for aircraft measurements at the Rio Branco AMAZONICA site (67.85°W, 9.19°S), just to the north of this region, during early 2011.

To isolate the wetland component of the seasonal cycle we subtract the NoWetlands model simulation (Fig. 5 (bottom)). Large anomalies in the seasonal cycle coincide with the peak of the wetland emissions in the models, suggesting that it is these wetland emissions that are being under-estimated.

Analysis of the GRACE Terrestrial Water Storage (TWS) and MODIS imagery (Fig. 6) show that the three years of highest CH$_4$ discrepancy (2010, 2011 and 2014) have strong seasonal cycles in above ground water storage. The MODIS imagery and analysis of the spatial distribution of the GRACE data (not shown) imply that the majority of the water mass anomalies follow the river channels (as discussed in Hamilton et al., 2004). This is particularly evident for the Bolivian wetlands in 2014. The years 2010 and 2011 are consistent with the increased precipitation during the 2010/2011 La Niña (Gloor et al., 2013). The models assessed here are failing to reproduce these large
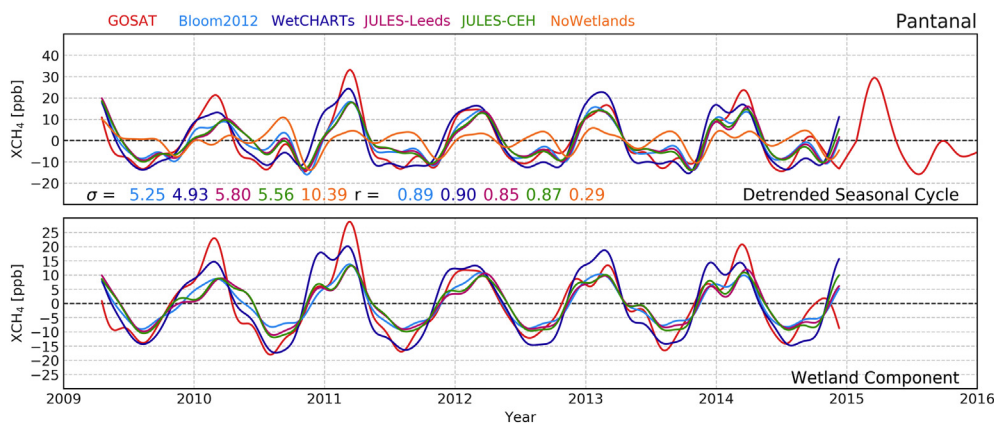

Fig. 5. Timeseries showing the detrended seasonal cycle over the Pantanal region, including the GOSAT observations and the model simulations utilising the different wetland emission datasets (top panel). The lower panel shows the difference to the NoWetlands model simulation (that does not contain any wetland emissions), providing information on the wetland component in each of the model simulations.
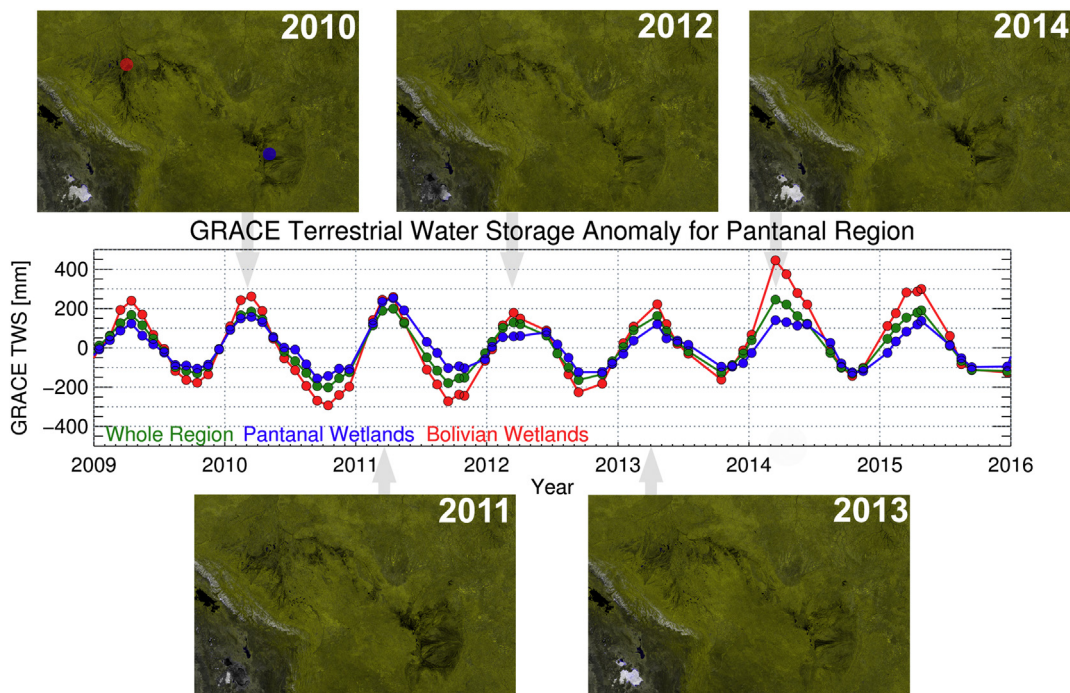
Fig. 6. Timeseries for the GRACE Terrestrial Water Storage Anomaly over the entire "Pantanal" region (green) as well as sampled at the centre of the Pantanal (blue) and Bolivian (red) wetland regions. MODIS imagery (RGB false-colour composite from the surface reflectance in bands 1 and 2) for February–April for each year is also included, highlighting the change in visible wetland extent between these years. (For interpretation of the references to colour in this figure legend, the reader is referred to the web version of this article.)
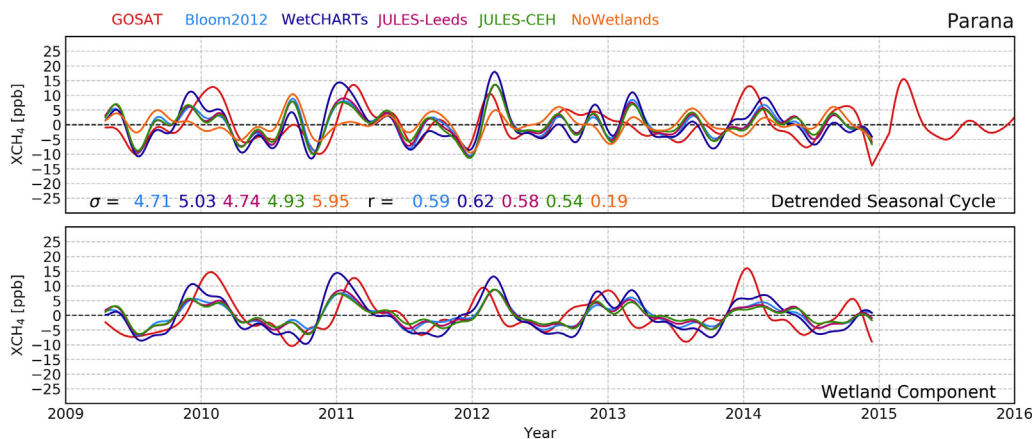
Fig. 7. Timeseries showing the detrended seasonal cycle over the Paraná region, including the GOSAT observations and the model simulations utilising the different wetland emission datasets (top panel). The lower panel shows the difference to the NoWetlands model simulation (that does not contain any wetland emissions), providing information on the wetland component in each of the model simulations.

scale, river fed, wetlands and as such are missing a large portion of the methane emissions in these regions.

Interestingly the year of largest water mass anomaly (2014) does not correspond to the year of largest CH_4 anomaly (2011). This could be due to the extreme 2014 flooding event exceeding the optimum conditions for net CH_4 emission, i.e. the depth of water above the surface is large enough to oxidise the CH_4 before it is emitted.

7.2. Paraná

The "Paraná" region in this analysis extends from the Iberá wetlands in northern Argentina (the world's second largest wetlands after the Pantanal), following the Paraná River south until it merges with the Uruguay River, forming the Río de la Plata (or River Plate) estuary which then discharges into the Atlantic Ocean. It is one of the most

important fluvial systems in South America (Marchetti et al., 2013). This region extends between 65°W to 52°W and 35°S to 25°S. The seasonal cycle of CH_4 in this region (Fig. 7 - top panel) is relatively strong, with values for the GOSAT seasonal cycle amplitude over the 5 years between 15.85–30.08 ± 3.96 ppb. All model simulations exhibit a similar seasonal cycle, peaking during the wet season at the start of each year. The models capture the magnitude and seasonality of the observations, but disagree in the timing of the onset of the positive phase of the seasonal cycle. Additionally, there are several anomalous events which we analyse in more detail.

The wetland component for the years 2010 and 2014 shows strong differences between the model simulations and the observations (Fig. 7 (bottom panel)). This indicates that all four of the wetland emission estimates fail to reproduce the CH_4 observations in these years. There is much better agreement between the observations and the simulations
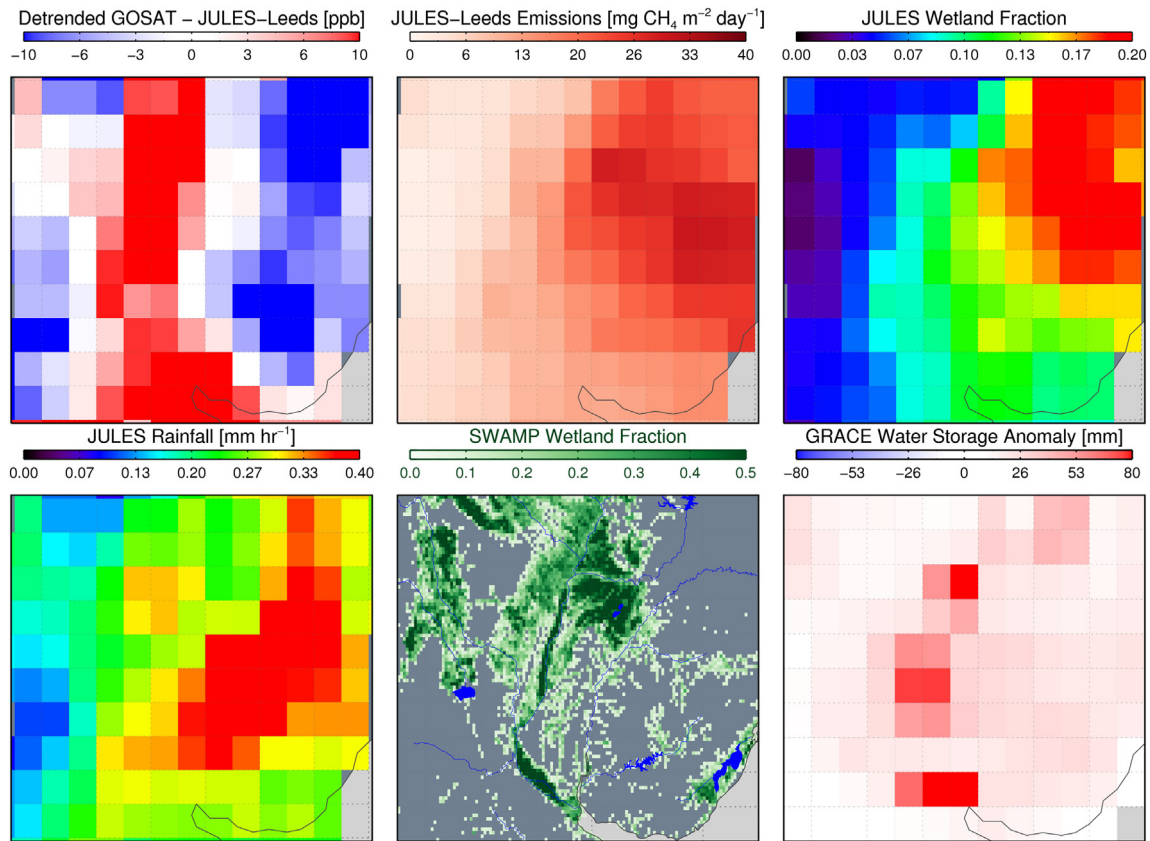
Fig. 8. Maps of the Paraná region for November 2009 to February 2010 showing (top-left, clock-wise): GOSAT-JULES-Leeds difference, JULES-Leeds wetland emissions, JULES wetland fraction, GRACE Water Storage Anomaly, SWAMP wetland fraction and JULES rainfall amount.

for other years, albeit the discrepancy in phase remains (e.g. model simulations peaking too early in 2011 and too late in 2012).

We focus on the early 2010 anomaly when the Paraná River experienced an "extraordinary" flooding event (Marchetti et al., 2013; Puig et al., 2016). The GOSAT - JULES-Leeds CH_4 difference is calculated between 1st November 2009 and 28th February 2010. These 647

measurements are subsequently averaged into $2° \times 2°$ boxes (Fig. 8 (top left)). The large anomaly following the course of the river indicate that the simulation is missing significant emissions in this region. The modelled emission (top centre) and wetland fraction (top right) indicate that JULES primarily places the wetlands (and consequently, the emissions) to the east of the region. This is where the rainfall occurs
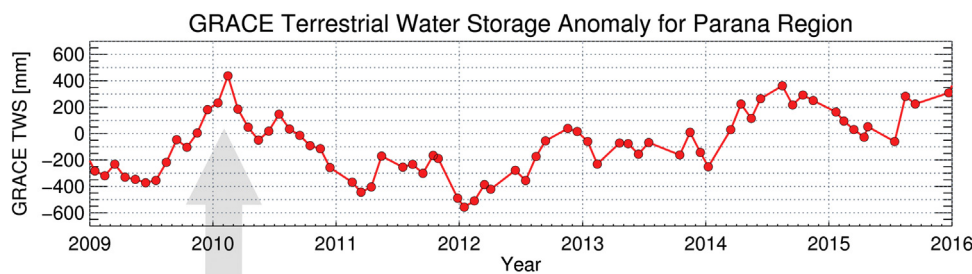

Fig. 9. Timeseries for the GRACE Terrestrial Water Storage Anomaly at the location indicated by the red circle along with MODIS imagery (RGB false-colour composite from the surface reflectance in bands 1 and 2) for January 2010 and 2011, showing the entire Paraná region. (For interpretation of the references to colour in this figure legend, the reader is referred to the web version of this article.)
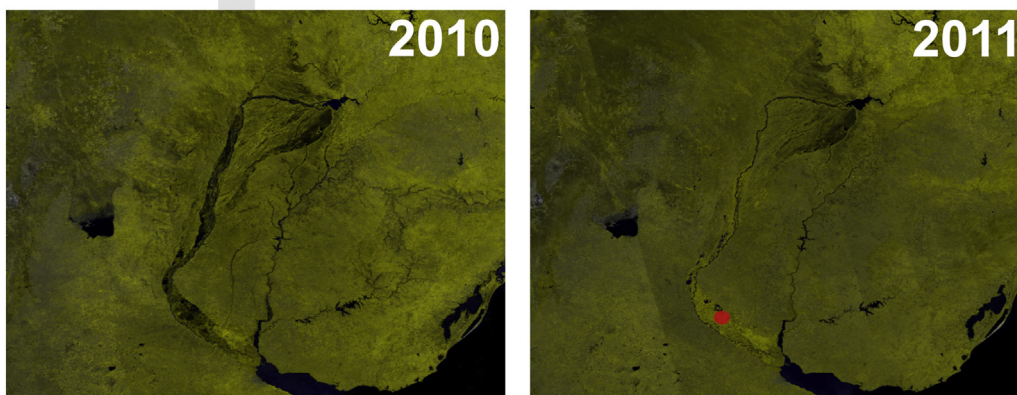
(bottom left). The SWAMP data (bottom centre) place the wetlands more centrally in the investigation region. The differences in wetland distribution matches the differences seen in the distribution of atmospheric CH_4. Even accounting for the incorrect placement of the wetlands, the overall magnitude of the wetland emissions from JULES is significantly lower than that suggested by the observations. Our proposed reason for this is shown by analysis of the GRACE terrestrial water storage anomaly (Fig. 8 (bottom right)), confirming a significant enhancement in the observed mass anomaly (i.e. water) along the banks of the Paraná River during January/February 2010.

Time-series of the GRACE TWS anomaly and MODIS imagery (Fig. 9) both show extreme levels of flooding in January 2010. January/February 2010 exhibited a large positive peak in the GRACE data, exceeding 500 mm, with values for the same time period in subsequent years typically below 0 mm. Many previous studies (Depetris et al., 1996; Amarasekera et al., 1997; Boulanger et al., 2005; Pasquini and Depetris, 2007, 2010) have identified the hydrology of the Paraná River and the Paraná-Plata basin as being sensitive to ENSO dynamics. Unlike the Amazon where excess river levels are driven by precipitation during the cold La Niña phase of ENSO, the Paraná River system exhibits flooding significantly correlated to the warm El Niño phase of ENSO (Depetris et al., 1996).

For the 2014 anomaly, observations show a strong CH_4 enhancement along the length of the Paraná River with the strongest enhancement directly over the Iberá wetlands. This is consistent with both GRACE and MODIS data which indicate an increase in the wetland extent during this time period. This is not reproduced in the JULES simulations and provides clear evidence that the process leading to wetland formation in this region, i.e. overbank inundation, is not sufficiently reproduced by JULES.

Overbank inundation describes the process whereby water is transported long distances via rivers, then re-enters the soil column downstream to create wetlands. Such wetlands could be induced by large floods following extreme rainfall events, as seen in 2010, as well as more continuously river-fed inundation regions as shown for the Bolivian wetlands (Section 7.1). The absence of this process means that a large portion of CH_4 emissions are missed by the simulations, and the potential impacts on future climate forcing are unaccounted for.

8. Evaluating emission estimates

To assess the significance of these anomalies on the regional CH_4 budget, we calculate the integrated annual seasonal cycle signal for each model simulation as a percentage of the GOSAT signal. We use these values to estimate the additional emissions required in each simulation to match the observations. This pragmatic approach to estimate the flux differences without the use of a full inversion system

makes the assumptions that the differences are due to wetland emissions and not for example, propagation of signals from the northern hemisphere.

Table 1 shows these values for the Pantanal and Parana regions, with both exhibiting similar behaviour. JULES-Leeds, JULES-CEH and Bloom2012 all underestimate the emissions compared to the observations and this discrepancy is larger in years with significant wetland flooding events.

For the exceptionally strong La Niña in 2011, these three models only emit 48–61% of the required wetland CH_4 to reproduce observations over the Pantanal region, a deficit of between 4.9–8.4 Tg yr^{-1}. For 2010, the year with significant overbank inundation of the Paraná River leading to an extensive area of wetlands not captured by the models, we find that the JULES-based emission estimates only provide 67–69% of the required emissions, a deficit of 4.4–4.5 Tg yr^{-1}. Despite incorporating GRACE data, the Bloom2012 estimates show a larger disagreement, under-predicting the seasonal cycle by 43% and requiring an additional 5.8 Tg yr^{-1} to match the observations.

In both regions, the closest estimates to the total required emissions are the WetCHARTs data (86–141%) but these emissions have the wrong temporal signal, peaking too early and not capturing the full extent of the observed cycles. Since WetCHARTs is the mean of multiple ensemble models, there is potential for future work to evaluate individual ensemble members to determine whether a change to a certain process (e.g. temperature, carbon, water or extent) leads to an improved performance.

9. Discussion

We identify regions that contain a significant wetland seasonal cycle compared to the signals from anthropogenic, rice and fire emissions (Pantanal, Paraná, Yucatán and Southern Africa) and analyse these in more detail.

For Paraná, we observed a significant difference between the simulations and observations in 2010. We have attributed this to the extensive flooding of the Paraná river caused by an excess of ENSO-driven precipitation. This substantially increased the extent of active methanogenesis during the 2010 wet season. Increases in wetland extent also occurred during 2011 for the Pantanal wetlands, 2014 in the Iberá and Llanos de Moxos wetlands, 2010/2013 in the wetlands of the Yucatán region, and annually for the seasonally inundated grasslands of Southern Africa. Such flood events are not reproduced by JULES because the model currently has no process to simulate wetlands fed via flooded rivers. In JULES when run-off water enters the river system it does not leave until it reaches the ocean, and JULES is susceptible to missing the emissions from such extreme events. Dadson et al. (2010) demonstrated improved estimates of evaporative fluxes and water

Table 1
Table showing the annual wetland component of the CH_4 seasonal cycle in % relative to the GOSAT value for each model simulation for the Pantanal and Paraná regions. A value of 100% indicates that the integrated wetland seasonal cycle signal is the same between the model and observations. A value less than 100% indicates that the model has a lower integrated wetland seasonal cycle than GOSAT. We also include the absolute change in emissions (in Tg yr^{-1}) that would need to be added to the simulations to match the observations.

	2010		2011		2012		2013		2014	
	%	ΔTg yr^{-1}	%	ΔTg yr^{-1}	%	ΔTg yr^{-1}	%	ΔTg yr^{-1}	%	ΔTg yr^{-1}
Pantanal										
JULES-Leeds	64%	4.4	56%	5.7	64%	4.1	60%	4.5	56%	5.4
JULES-CEH	69%	3.8	61%	4.9	69%	3.5	66%	3.9	61%	4.5
Bloom2012	53%	6.8	48%	8.4	64%	4.1	57%	6.2	52%	6.7
WetCHARTs	94%	0.5	95%	0.4	114%	−0.9	98%	0.15	94%	0.5
Paraná										
JULES-Leeds	67%	4.5	62%	3.6	86%	1.8	61%	4.5	56%	4.8
JULES-CEH	69%	4.4	71%	3.2	81%	1.3	65%	4.3	46%	7.3
Bloom2012	57%	5.8	65%	4.2	102%	−0.2	60%	5.1	55%	6.3
WetCHARTs	93%	0.6	109%	−0.6	141%	−2.2	102%	−0.2	86%	1.1

budgets when overbank inundation was included in JULES on the regional scale. Our work indicates that inclusion of this process will have a significant impact on estimates of CH_4 emissions and, therefore, the potential feedbacks on climate forcing. Ongoing work by Marthews (in preparation) will add overbank inundation to JULES which should help address this issue. Previous work to improve JULES CH_4 emission fluxes focusing on transport mechanisms, like those described by Pangala et al. (2017) have not improved spatial and temporal representation of fluxes (McNorton et al., 2016b); however, improved process descriptions in the future might be key in certain regions not explored in this study.

Previous work (Melton et al., 2013) has shown that wetland extent calculations can vary dramatically between different LSMs (with yearly maximum wetland extent ranging between 7 and 27 M km ^{2}), hence identifying the mechanisms that drive such variability and evaluating them can lead to significant improvements in estimating wetland extent. Many LSMs rely on a topography-based hydrological model in their generation of wetlands. As some regions (such as the Pantanal) are very flat and have a low standard deviation of topographic index, they are prone to failure of the TOPMODEL methodology, particularly when run-off/river water is not sufficiently transported laterally. This very low standard deviation of terrain means that the water table has to be very close to the surface before wetland starts to form (Gedney et al., 2004). Furthermore, much of the water feeding these wetlands is from rivers and not adequately modelled by JULES, resulting in insufficient water to raise the water table.

Top-down estimates for wetland CH_4 missions from the Bloom2012 data (which itself utilises GRACE data in its generation of wetland extent) also fails to capture the magnitude of the emissions, likely due to the low spatial resolution ($3° \times 3°$) of the Bloom2012 dataset or issues with the diagnostic model parametrisation not capturing the extent of the anomalies. We recognise the importance of top-down estimates and future work to extend and improve such estimates would be of benefit.

We find that, as expected, flooding in South America coincides with precipitation driven by the La Niña (for the Pantanal) and El Niño (for the Paraná) phases of the ENSO system. Thus CH_4 inter-annual variability is sensitive to future changes in ENSO dynamics. For such events, we calculate that the under-estimation of the wetland extent, previously recognised as a significant contribution to uncertainties in CH_4 wetland emissions (Ringeval et al., 2010; Bohn et al., 2015; Saunois et al., 2016), leads to an underestimation of emissions by more than 50%, resulting in a deficit of 5.3–11.8 Tg yr^{-1} from these two regions alone.

10. Conclusion

Globally, we found that the latitudinal means of the detrended seasonal cycle agree well between simulations and observations, with average differences between 1.7–2.7 ppb but with maximum differences in the tropics of 28.1–34.8 ppb, suggesting that all simulations fail to capture the full extent of the tropical wetland seasonal cycle.

We have verified that a major driver for year-to-year anomalies in tropical CH_4 wetland emissions is seasonal flooding, often related to river overbanking and linked to ENSO variability. Current LSMs generally lack such an overbank inundation mechanism and are therefore not capable of capturing the temporal or spatial variability in the CH_4 seasonal cycle. This leads to an underestimate of the emissions by 17.1–24.3 Tg yr^{-1} totalled over the four regions examined in this study.

Furthermore we have successfully shown the utility in a range of earth observation data for successfully evaluating the temporal/spatial distribution of wetland extent and informing the development of such LSMs.

Future observations of atmospheric XCH_4, such as those from the Sentinel 5-Precursor (Hu et al., 2016) and the NASA GeoCARB (Polonsky et al., 2014) missions, will be obtained at an unprecedented spatial and temporal resolution and along with new missions to measure precipitation (NASA's Global Precipitation Measurement, Hou et al., 2014), plant biomass (BIOMASS, Quegan et al., 2012) and vegetation dynamics (FLEX, Drusch et al., 2017), the capability to evaluate the skill of current and future land surface (and coupled-climate) models will advance further, improving our understanding and predictive capability related to these important climate-significant processes.

Appendix A. JULES wetland CH$_4$ emission estimates

Natural CH$_4$ emissions from wetlands, F_{CH_4}, are estimated in JULES following Gedney et al. (2004) at a prescribed spatial discretisation by:

$$F_{CH_4} = k_{CH_4} f_w \Lambda Q_{10} (T_{soil})^{(T_{soil}-T_0)/10}$$ (A.1)

where f_w is the fraction of a gridbox where the water table is at or slightly above the surface. Λ (kg CH$_4$ m^{-2} s^{-1}) is the sum of the carbon mass in each of the soil carbon pools (decomposable plant matter, resistant plant matter, biomass and long-lived humus) weighted by their respective respiration rate. The carbon mass of each soil carbon pool is a prognostic of the TRIFFID dynamic vegetation model, therefore providing another aspect of seasonality to the simulated emission. Q_{10} is a factor parametrising the temperature dependence of the methanogenesis rate, T_{soil} (K) is soil temperature, T_0 (K) is a reference temperature and k is a calibration constant (Gedney and Cox, 2003). The value of k has been selected such that the global mean emission estimates are 175 Tg yr^{-1} between 2000 and 2009, consistent with the work in Ciais et al. (2013).

Within JULES f_w is calculated as the integral of a Gamma distribution of topographic index, τ_{index}, between the minimum and maximum critical limits, i.e.:

$$f_w = \int_{(\tau_{min})}^{(\tau_{max})} G(\tau)$$ (A.2)

where G is the gamma distribution form as described by Sivapalan et al. (1987). τ_{min} defines where the water table is at or above the surface and is dependent on the current mean water table depth, ($\overline{z_w}$ (m)), that is:

$$\tau_{min} = \ln \frac{\Psi(0)}{\Psi(\overline{z_w})} + \overline{\tau}$$ (A.3)

where $\Psi(0)$ and $\Psi(\overline{z_w})$ are the local transmissivities of the entire soil column and the soil column below the water table, respectively. τ_{max} defines where the water table rises sufficiently above the surface to induce streamflow and is no longer considered to emit methane, it is calculated as a constant increment to τ_{min}, i.e.:

$$\tau_{max} = \tau_{min} + \tau_{range}$$ (A.4)

For further details on the JULES implementation of TOPMODEL please refer to Gedney and Cox (2003), Marthews et al. (2015).

The two JULES wetland emission estimates used in this study (JULES-Leeds and JULES-CEH) use different parameters for the same equations and consequently using both provides an estimate of uncertainty. The primary differences between these two model setups have been summarised in Table A.2. JULES-Leeds considers only the top 10 cm of the soil column for the temperature dependency of methanogenesis and, hence, has a lower Q_{10} value, optimised to give best agreement with surface CH$_4$ flux observations over large scales in time and space (Gedney et al., 2004; McNorton et al., 2016b). Thus, one would expect JULES-Leeds to respond stronger to temperature fluctuations (since soil temperature variation is dampened with depth). Additionally, JULES-Leeds and JULES-CEH have different values of τ_{range} in their TOPMODEL setup (Table A.2). This difference means the JULES-CEH configuration can produce a larger fractional cover of wetland per gridbox than the JULES-Leeds setup. These differences result in a higher sensitivity of JULES-Leeds to changes in precipitation and temperature, allowing predictions of larger regions of active methanogenesis.

JULES can be run as a stand-alone model or as the land-surface component of coupled climate models (e.g. HadCM3 (Walters et al., 2011) and the UK Earth System Model (UKESM)). Note that the JULES-CEH wetland and CH$_4$ emission configuration will be used in the UKESM.

Table A.2
Primary differences, with respect to wetland CH$_4$ emissions, in tuning of the JULES-Leeds and JULES-CEH model parametrisations.

	JULES-Leeds	JULES-CEH
T_{soil} depth	0.1 m	1 m
$Q_{10}(T_0)$	3.0	3.7
τ_{index} wetland range	2.0	1.5

Appendix B. Global CH$_4$ distribution

This section provides extra details on the zonal mean comparisons described in Section 6 as well as a Hovmoller plot (Fig. B.1) showing the different distributions.

These maximum differences between the simulations and GOSAT in the tropics are found to be 28.1 ppb (JULES-Leeds), 28.1 ppb (JULES-CEH), 34.5 ppb (Bloom2012) and 34.8 ppb (WetCHARTs), suggesting that all of the model simulations fail to capture the full extent of the tropical wetland seasonal cycle. Large negative differences (i.e. model seasonal cycle is higher than observations) are found both in the 10°N–40° N latitude band (with minimum values ranging from −24.6 to −25.3 ppb for the different simulations) as well as a second, summertime band at high northern latitudes, greater than 60°N (with minimum value ranging from −60.0 to −74.3 ppb). These are respectively attributable to over-estimation of anthropogenic and rice emissions in Asia and boreal wetland emissions.
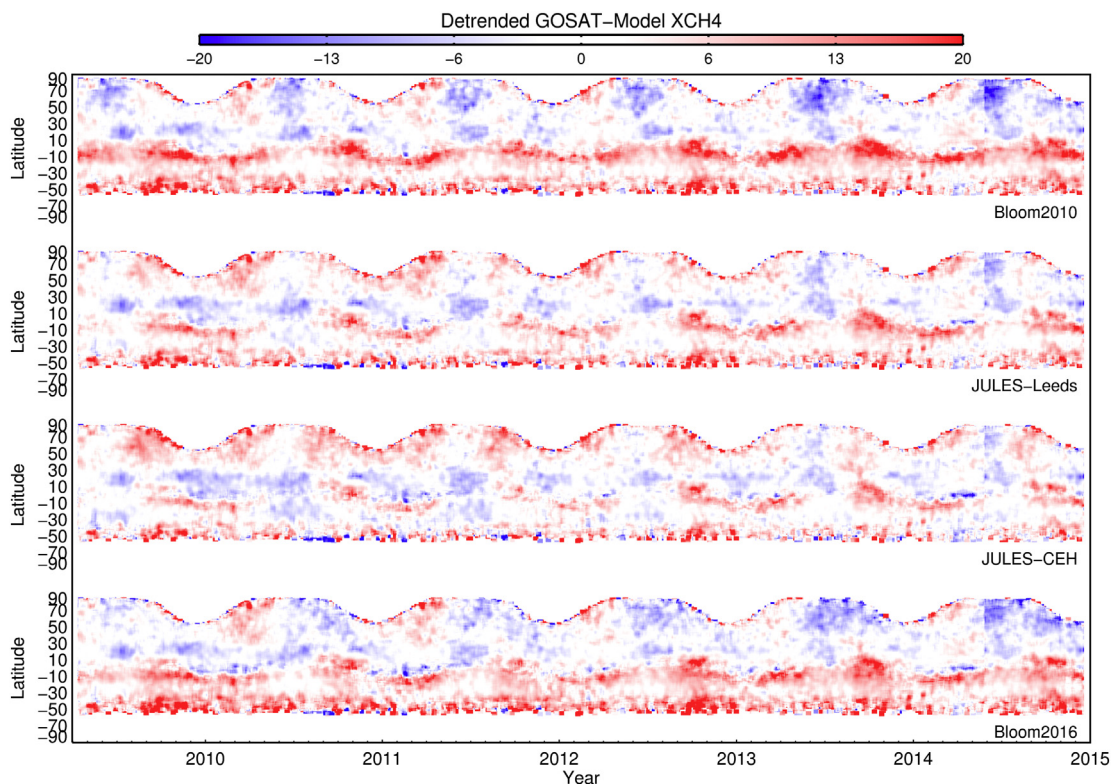
Fig. B.1. Hovmoller plot showing the difference between the GOSAT and model seasonal cycles for each model simulation between 2009 and 2014.

Appendix C. Calculation of integrated emission signal

We integrate the detrended seasonal cycle signal between minima for GOSAT and each simulation. An example of this for the Pantanal region is shown in Fig. C.1. Ratioing these integrated values to the GOSAT value allows the difference in emissions (in Tg yr^{-1}) to be calculated.
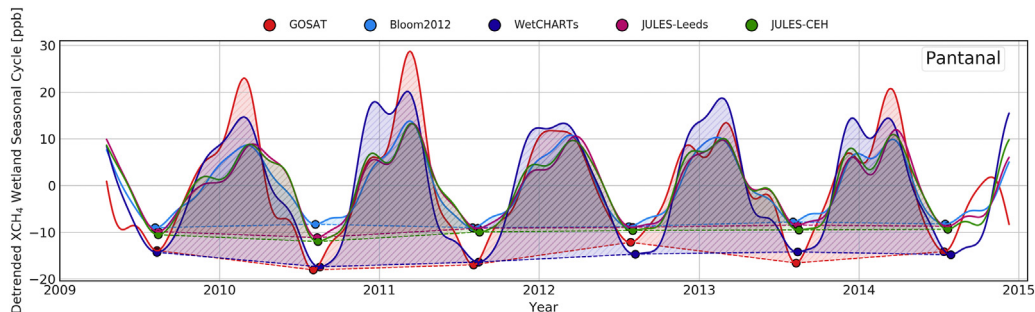

Fig. C.1. An example of the integrated seasonal cycle calculation for the Pantanal region.

Appendix D. Additional regional analysis

Table D.1
Table showing the annual wetland component of the CH$_4$ seasonal cycle in % relative to the GOSAT value for each model simulation for the Yucatán and Southern Africa regions. A value of 100% indicates that the integrated wetland seasonal cycle signal is the same between the model and observations. A value less than 100% indicates that the model has a lower integrated wetland seasonal cycle than GOSAT. We also include the absolute change in emissions (in Tg yr^{-1}) that would need to be added to the simulations to match the observations.

	2010		2011		2012		2013		2014	
	%	ΔTg yr^{-1}	%	ΔTg yr^{-1}	%	ΔTg yr^{-1}	%	ΔTg yr^{-1}	%	ΔTg yr^{-1}
Yucatán										
JULES-Leeds	91%	0.8	102%	−0.1	67%	4.5	54%	4.5	N/A	N/A
JULES-CEH	63%	4.9	77%	2.3	79%	2.4	80%	1.9	N/A	N/A
Bloom2012	79%	2.0	82%	1.7	42%	10.7	56%	6.1	N/A	N/A
WetCHARTs	148%	−2.4	153%	−2.4	78%	2.1	89%	0.9	N/A	N/A

Southern Africa										
JULES-Leeds	48%	8.4	48%	7.9	38%	13.4	38%	10.8	37%	11.2
JULES-CEH	44%	9.3	42%	10.6	38%	14.2	41%	10.9	38%	12.4
Bloom2012	55%	5.9	59%	6.4	51%	6.4	51%	8.9	47%	6.9
WetCHARTs	56%	4.7	57%	5.5	54%	6.8	151%	7.1	45%	9.4

In the main text we focus on the South American regions where natural wetlands dominate the seasonal cycle and the wetland inter-annual variability is particularly sensitive to ENSO variability. In this section, we also show that similar behaviour can be identified for other regions that exhibit a strong wetland seasonal cycle, namely Yucatán and Southern Africa.

D.1. Yucatán

In this section, we examine the seasonal cycle signal over the Yucatán peninsula area of Mexico, with particular focus on the Tabasco and Campeche wetlands at the northern base of the peninsula. The Tabasco area contains the large Reserva de la Biosfera Pantanos de Centla, consisting of primarily flooded freshwater swampland. The nearby Campeche region also contains the largest coastal lagoon on the Mexican shore of the Gulf of Mexico, supporting in excess of 120,000 ha of mangrove forests. Fig. D.1 shows the full "Yucatán" region used in this analysis, with the SWAMP wetland data indicating the location and types of wetlands present. The Tabasco and Campeche wetlands described above are clearly visible on the northern coast at the base of the Yucatán Peninsula.
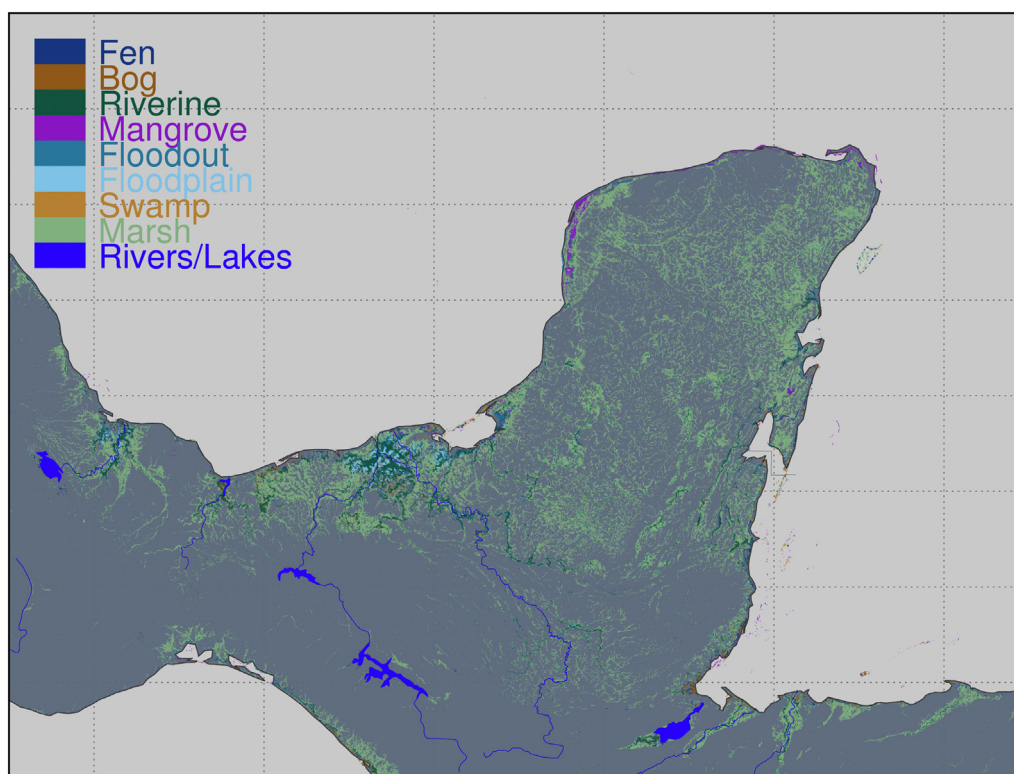

Fig. D.1. SWAMP wetland data showing the location and type of wetlands present in the Yucatán Peninsula region.

When examining the CH_4 seasonal cycle for this region, we find that all of the model simulations do a reasonable job in capturing the general magnitude and phase (standard deviation ranging from 4.16 to 5.16 ppb and the correlation coefficient ranging from 0.64 to 0.78). However, when examining the wetland component in isolation, the wetland seasonal cycle is too weak compared to observations in all of the simulations for the peak in wetland activity during September-November each year. In particular, 2010 and 2013 show the largest discrepancies against the model.

For 2010, the wetland GOSAT signal peaks at 13.88 ppb, compared to model values of 5.27 ppb (JULES-Leeds), 3.52 ppb (JULES-CEH), 3.62 ppb (Bloom2012) and 9.29 ppb (WetCHARTs), with WetCHARTs the only simulation approaching a similar magnitude to GOSAT. For 2013, all of the model simulations have a peak of less than 6 ppb (4.51–5.77 ppb), compared to a peak in the GOSAT data of almost 17.91 ppb. This suggests that all of the emission estimates are missing a large wetland signal in this region. Again, analysis of the GRACE data for this area shows that 2010 and 2013 were both anomalous years, with the TWS in excess of 700 mm, compared to values of between 200–400 mm for the other years. The anomaly in both the GOSAT-JULES difference and the GRACE satellite data are geographically consistent with the Tabasco/Campeche wetland areas, indicating that it is this region driving the anomalies in the timeseries. The normalised integrated seasonal cycle signal for this region suggests that for 2013, all the emission estimates underestimate the required emissions, with values ranging from 37%–48% of the observed signal.

D.2. Southern Africa

Here, we analyse in detail the region of Southern Africa, defined as 15˚E to 33˚E and 22˚S to 8˚S. This region encompasses wetlands, primarily swampland and seasonally inundated grassland, in Zambia, Angola and Botswana. Although for this region both the modelled wetland and

anthropogenic seasonal cycle magnitudes are comparable at ∼ 10 ppb, the fact that they are distinctly out of phase (with the wetland signal peaking in March/April and the anthropogenic signal peaking in July/August) means that we can successfully identify and assess the peak in the wetland component.

The behaviour in this region is extremely systematic, despite the phase being in good agreement, the peak from wetland emissions in the model simulations are significantly lower than that of the observations. The maximum values of the GOSAT seasonal cycle range from 9.91–16.25 ± 1.74 ppb over the 5 years. The JULES-based simulations are significantly lower than this, ranging from 5.95–8.65 ± 1.87 for JULES-Leeds and 5.54–8.31 ± 1.87 for JULES-CEH. The two Bloom emission datasets for this region better reproduce the magnitude of the observed signal than JULES, having peaks in the range of 11.30–15.60 ± 2.04(Bloom2012) and 9.62–13.11 ± 1.97(WetCHARTs). The Bloom2012 simulation does the best at reproducing the observations, with a correlation coefficient of 0.83 and a standard deviation of 3.96 ppb, both significantly better than the other datasets. Overall, the observations suggest a peak to peak seasonal cycle magnitude of the wetland component of 22.47–27.07 ppb, compared to values for the simulations of 10.42–13.91 ppb (JULES-Leeds), 9.72–11.91 ppb (JULES-CEH), 14.28–16.62 ppb (Bloom2012) and 12.36–13.67 ppb (WetCHARTs).

Fig. D.2 shows the calculated JULES wetland fraction for March 2010 (left), along with the SWAMP wetland data (middle) and MODIS data (left). The JULES wetland fraction suggests that the majority of wetlands in this region are located to the north-east. However whilst the SWAMP data does show that this area contains the region's permanent water bodies, it also highlights that there is a large area of swampland and seasonally inundated wetland in the centre of this region which is not represented in the JULES data. As the SWAMP data is static in time, we also use the MODIS Normalized Difference Water Index (NDWI) which provides an indication of the water coverage in this region (Gao, 1996). Fig. D.2 (right) shows the MODIS visible image for February/March 2010, overlaid with the MODIS NDWI data for this time period in red and the NDWI for later in the year, during the dry season (August/September 2010) in blue. The blue areas therefore represent the permanent water bodies in this region and correspond to the known locations of rivers and lakes (as shown in the central figure), whereas the red areas indicate seasonal wetlands. Whilst there is clearly some indication of seasonally inundated wetlands in the north-east of this region, the large central wetland that is missing from the JULES data strongly features here, giving further confidence that JULES misses this significant wetland area, leading to it significantly under-estimating the seasonal cycle in this region (with annual normalised values ranging from 41% to 57% for JULES-Leeds and 39% to 53% for JULES-CEH). In contrast, the Bloom2012 emissions, which use the GRACE data to identify wetland areas, performs far better in this region and correctly assigns emissions to this central region (with annual normalised values ranging from 53% to 82%), indicating that correctly identifying the wetland extent in this region is key to better reproducing the observed seasonal cycle.
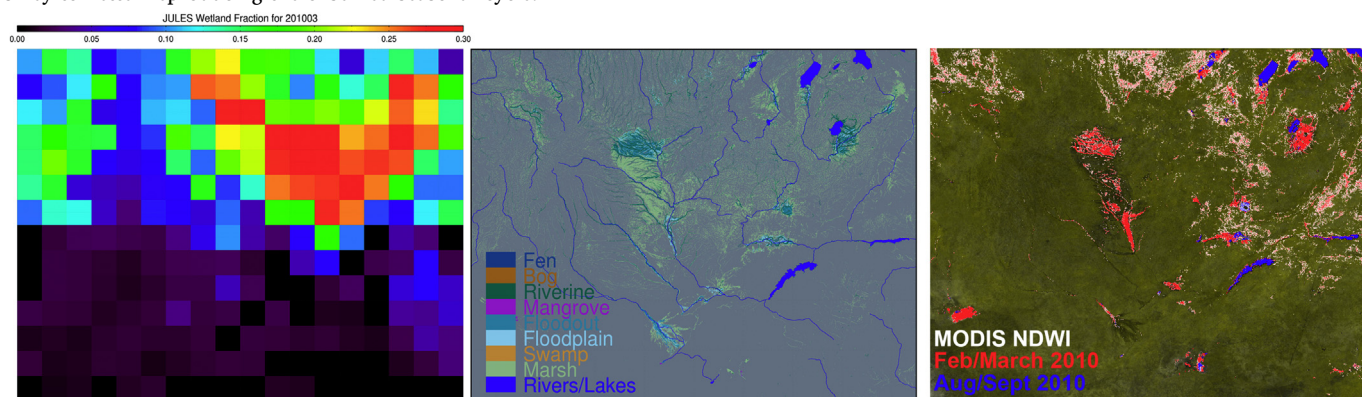

Fig. D.2. Maps for the Southern Africa region showing the JULES wetland fraction (left), the SWAMP wetland data (centre) and the MODIS visible imagery overlaid with NDWI for the wet (red) and dry (blue) seasons.

References

Alexe, M., Bergamaschi, P., Segers, A., Detmers, R., Butz, A., Hasekamp, O., Guerlet, S., Parker, R., Boesch, H., Frankenberg, C., Scheepmaker, R., Dlugokencky, E., Sweeney, C., Wofsy, S., Kort, E., 2015. Inverse modelling of CH4 emissions for 2010–2011 using different satellite retrieval products from GOSAT and SCIAMACHY. Atmos. Chem. Phys. 15 (1), 113–133.

Amarasekera, K.N., Lee, R.F., Williams, E.R., Eltahir, E.A., 1997. ENSO and the natural variability in the flow of tropical rivers. J. Hydrol. 200 (1), 24–39.

Best, M., Pryor, M., Clark, D., Rooney, G., Essery, R., Ménard, C., Edwards, J., Hendry, M., Porson, A., Gedney, N., et al., 2011. The Joint UK Land Environment Simulator (JULES), model description-part 1: energy and water fluxes. Geosci. Model Dev. 4 (3), 677–699.

Bloom, A.A., Palmer, P.I., Fraser, A., David, S.R., Frankenberg, C., 2010. Large-scale controls of methanogenesis inferred from methane and gravity spaceborne data. Science 327 (5963), 322–325.

Bloom, A., Palmer, P., Fraser, A., Reay, D., 2012. Seasonal variability of tropical wetland CH4 emissions: the role of the methanogen-available carbon pool. Biogeosciences 9 (8), 2821.

Bloom, A.A., Bowman, K.W., Lee, M., Turner, A.J., Schroeder, R., Worden, J.R., Weidner, R., McDonald, K.C., Jacob, D.J., 2017. A global wetland methane emissions and uncertainty dataset for atmospheric chemical transport models (WetCHARTs version 1.0). Geosci. Model Dev. 10, 2141–2156.

Bloom, A.A., Exbrayat, J.-F., van der Velde, I.R., Feng, L., Williams, M., 2016. The decadal state of the terrestrial carbon cycle: global retrievals of terrestrial carbon allocation, pools, and residence times. Proc. Natl. Acad. Sci. 113 (5), 1285–1290.

Boesch, H., Baker, D., Connor, B., Crisp, D., Miller, C., 2011. Global characterization of CO2 column retrievals from shortwave-infrared satellite observations of the orbiting carbon observatory-2 mission. Remote Sens. 3 (2), 270–304.

Bohn, T.J., Melton, J.R., Ito, A., Kleinen, T., Spahni, R., Stocker, B.D., Zhang, B., Zhu, X., Schroeder, R., Glagolev, M.V., Maksyutov, S., Brovkin, V., Chen, G., Denisov, S.N., Eliseev, A.V., Gallego-Sala, A., McDonald, K.C., Rawlins, M.A., Riley, W.J., Subin, Z.M., Tian, H., Zhuang, Q., Kaplan, J.O., 2015. WETCHIMP-WSL: intercomparison of wetland methane emissions models over West Siberia. Biogeosciences 12 (11), 3321–3349.

Bontemps, S., Defourny, P., Bogaert, E.V., Arino, O., Kalogirou, V., Perez, J.R., 2011. GLOBCOVER 2009-products description and validation report. In: Tech. rep.

Boulanger, J.-P., Leloup, J., Penalba, O., Rusticucci, M., Lafon, F., Vargas, W., 2005. Observed precipitation in the Paraná-Plata hydrological basin: long-term trends, extreme conditions and ENSO teleconnections. Clim. Dyn. 24 (4), 393–413.

Bousquet, P., Ciais, P., Miller, J.B., Dlugokencky, E.J., Hauglustaine, D.A., Prigent, C., Van Der Werf, G.R., Peylin, P., Brunke, E., Carouge, C., Langenfelds, R.L., Lathiere, J., Papa, F., Ramonet, M., Schmidt, M., Steele, L.P., Tyler, S.C., White, J., 2006. Contribution of anthropogenic and natural sources to atmospheric methane variability. Nature 443 (7110), 439–443.

Bousquet, P., Ringeval, B., Pison, I., Dlugokencky, E., Brunke, E.-G., Carouge, C., Chevallier, F., Fortems-Cheiney, A., Frankenberg, C., Hauglustaine, D., et al., 2011. Source attribution of the changes in atmospheric methane for 2006–2008. Atmos. Chem. Phys. 11 (8), 3689–3700.

Buchwitz, M., Reuter, M., Schneising, O., Hewson, W., Detmers, R.G., Boesch, H., Hasekamp, O.P., Aben, I., Bovensmann, H., Burrows, J.P., Butz, A., Chevallier, F., Dils, B., Frankenberg, C., Heymann, J., Lichtenberg, G., De Mazière, M., Notholt, J., Parker, R., Warneke, T., Zehner, C., Griffith, D.W.T., Deutscher, N.M., Kuze, A., Suto,

H., Wunch, D., 2017. Global satellite observations of column-averaged carbon dioxide and methane: the GHG-CCI XCO2 and XCH4 CRDP3 data set. Remote Sens. Environ. 203, 276–295.

Chipperfield, M.P., 2006. New version of the TOMCAT/SLIMCAT off-line chemical transport model: intercomparison of stratospheric tracer experiments. Q. J. R. Meteorol. Soc. 132 (617), 1179–1203.

Christensen, T.R., Ekberg, A., Ström, L., Mastepanov, M., Panikov, N., Öquist, M., Svensson, B.H., Nykänen, H., Martikainen, P.J., Oskarsson, H., 2003. Factors controlling large scale variations in methane emissions from wetlands. Geophys. Res. Lett. 30 (7), 1414.

Ciais, P., Sabine, C., Bala, G., Bopp, L., Brovkin, V., Canadell, J., Chhabra, A., DeFries, R., Galloway, J., Heimann, M., Jones, C., Le Quéré, C., Myneni, R., Piao, S., Thornton, P., 2013. Carbon and Other Biogeochemical Cycles. Cambridge University Press, Cambridge, United Kingdom and New York, NY, USA, pp. 465–570 Book Section 6.

Clark, D.B., Mercado, L.M., Sitch, S., Jones, C.D., Gedney, N., Best, M.J., Pryor, M., Rooney, G.G., Essery, R.L.H., Blyth, E., Boucher, O., Harding, R.J., Huntingford, C., Cox, P.M., 2011. The Joint UK Land Environment Simulator (JULES), model description- part 2: carbon fluxes and vegetation dynamics. Geosci. Model Dev. 4 (3), 701–722.

Cogan, A., Boesch, H., Parker, R., Feng, L., Palmer, P., Blavier, J.-F., Deutscher, N.M., Macatangay, R., Notholt, J., Roehl, C., Warneke, T., Wunch, D., 2012. Atmospheric carbon dioxide retrieved from the Greenhouse gases Observing SATellite (GOSAT): comparison with ground-based TCCON observations and GEOS-Chem model calculations. J. Geophys. Res. Atmos. (1984-2012) 117 (D21).

Comyn-Platt, E., Hayman, G.D., McNorton, J., Gedney, N., 2018. Monthly Global Methane Emissions From Natural Wetlands Modelled by JULES With Dynamic Vegetation (1980–2014) v1.0.

Cressot, C., Chevallier, F., Bousquet, P., Crevoisier, C., Dlugokencky, E.J., Fortems-Cheiney, A., Frankenberg, C., Parker, R., Pison, I., Scheepmaker, R.A., Montzka, S.A., Krummel, P.B., Steele, L.P., Langenfelds, R.L., 2014. On the consistency between global and regional methane emissions inferred from SCIAMACHY, TANSO-FTS, IASI and surface measurements. Atmos. Chem. Phys. 14 (2), 577–592.

Dadson, S.J., Ashpole, I., Harris, P., Davies, H.N., Clark, D.B., Blyth, E., Taylor, C.M., 2010. Wetland inundation dynamics in a model of land surface climate: evaluation in the Niger inland delta region. J. Geophys. Res. Atmos. 115 (D23) n/a-n/a, D23114.

Depetris, P.J., Kempe, S., Latif, M., Mook, W.G., 1996. ENSO-controlled flooding in the Paraná River (1904–1991). Naturwissenschaften 83 (3), 127–129.

Dils, B., Buchwitz, M., Reuter, M., Schneising, O., Boesch, H., Parker, R., Guerlet, S., Aben, I., Blumenstock, T., Burrows, J.P., Butz, A., Deutscher, N.M., Frankenberg, C., Hase, F., Hasekamp, O.P., Heymann, J., De Mazière, M., Notholt, J., Sussmann, R., Warneke, T., Griffith, D., Sherlock, V., Wunch, D., 2014. The greenhouse gas climate change initiative (GHG-CCI): comparative validation of GHG-CCI SCIAMACHY/ ENVISAT and TANSO-FTS/GOSAT CO2 and CH4 retrieval algorithm products with measurements from the TCCON. Atmos. Meas. Tech. 7 (6), 1723–1744.

Dlugokencky, E.J., Bruhwiler, L., White, J.W.C., Emmons, L.K., Novelli, P.C., Montzka, S.A., Masarie, K.A., Lang, P.M., Crotwell, A.M., Miller, J.B., Gatti, L.V., 2009. Observational constraints on recent increases in the atmospheric CH4 burden. Geophys. Res. Lett. 36 (18).

Dlugokencky, E.J., Houweling, S., Bruhwiler, L., Masarie, K.A., Lang, P.M., Miller, J.B., Tans, P.P., 2003. Atmospheric methane levels off: temporary pause or a new steady-state? Geophys. Res. Lett. 30 (19).

Drusch, M., Moreno, J., Del Bello, U., Franco, R., Goulas, Y., Huth, A., Kraft, S., Middleton, E.M., Miglietta, F., Mohammed, G., et al., 2017. The FLuorescence EXplorer Mission Concept–ESA's Earth Explorer 8. IEEE Trans. Geosci. Remote Sens. 55 (3), 1273–1284.

Etminan, M., Myhre, G., Highwood, E.J., Shine, K.P., 2016. Radiative forcing of carbon dioxide, methane, and nitrous oxide: a significant revision of the methane radiative forcing. Geophys. Res. Lett. 43 (24), 12,614–12,623 2016GL071930.

Frankenberg, C., Meirink, J.F., Bergamaschi, P., Goede, A.P.H., Heimann, M., Körner, S., Platt, U., van Weele, M., Wagner, T., 2006. Satellite chartography of atmospheric methane from SCIAMACHY on board ENVISAT: analysis of the years 2003 and 2004. J. Geophys. Res. Atmos. 111 (D7) D07303.

Fraser, A., Chan Miller, C., Palmer, P.I., Deutscher, N.M., Jones, N.B., Griffith, D.W.T., 2011. The Australian methane budget: interpreting surface and train-borne measurements using a chemistry transport model. J. Geophys. Res. Atmos. 116 (D20) D20306.

Fraser, A., Palmer, P.I., Feng, L., Boesch, H., Cogan, A., Parker, R., Dlugokencky, E.J., Fraser, P.J., Krummel, P.B., Langenfelds, R.L., O'Doherty, S., Prinn, R.G., Steele, L.P., van der Schoot, M., Weiss, R.F., 2013. Estimating regional methane surface fluxes: the relative importance of surface and GOSAT mole fraction measurements. Atmos. Chem. Phys. 13 (11), 5697–5713.

Fraser, A., Palmer, P.I., Feng, L., Bösch, H., Parker, R., Dlugokencky, E.J., Krummel, P.B., Langenfelds, R.L., 2014. Estimating regional fluxes of CO2 and CH4 using space-borne observations of XCH4: XCO2. Atmos. Chem. Phys. 14 (23), 12883–12895.

Gao, B.-C., 1996. NDWI–a normalized difference water index for remote sensing of vegetation liquid water from space. Remote Sens. Environ. 58 (3), 257–266.

Gedney, N., Cox, P.M., 2003. The sensitivity of global climate model simulations to the representation of soil moisture heterogeneity. J. Hydrometeorol. 4 (6), 1265–1275.

Gedney, N., Cox, P.M., Huntingford, C., 2004. Climate feedback from wetland methane emissions. Geophys. Res. Lett. 31 (20) L20503.

Gedney, N., Huntingford, C., Comyn-Platt, E., 2017. Raised Global Wetland Methane Emissions Under Climate Change. in preparation.

Gloor, M., Brienen, R.J.W., Galbraith, D., Feldpausch, T.R., Schöngart, J., Guyot, J.-L., Espinoza, J.C., Lloyd, J., Phillips, O.L., 2013. Intensification of the Amazon hydrological cycle over the last two decades. Geophys. Res. Lett. 40 (9), 1729–1733.

Gumbricht, T., Roman-Cuesta, R.M., Verchot, L., Herold, M., Wittmann, F., Householder,

E., Herold, N., Murdiyarso, D., 2017. An expert system model for mapping tropical wetlands and peatlands reveals south america as the largest contributor. Glob. Chang. Biol. 23 (9), 3581–3599.

Hamilton, S.K., Sippel, S.J., Melack, J.M., 2004. Seasonal inundation patterns in two large savanna floodplains of South America: the Llanos de Moxos (Bolivia) and the Llanos del Orinoco (Venezuela and Colombia). Hydrol. Process. 18 (11), 2103–2116.

Hayman, G., O'Connor, F., Dalvi, M., Clark, D., Gedney, N., Huntingford, C., Prigent, C., Buchwitz, M., Schneising, O., Burrows, J., et al., 2014. Comparison of the HadGEM2 climate-chemistry model against in situ and SCIAMACHY atmospheric methane data. Atmos. Chem. Phys. 14 (23), 13257–13280.

Hodson, E.L., Poulter, B., Zimmermann, N.E., Prigent, C., Kaplan, J.O., 2011. The El Niño-Southern oscillation and wetland methane interannual variability. Geophys. Res. Lett. 38 (8) L08810.

Hou, A.Y., Kakar, R.K., Neeck, S., Azarbarzin, A.A., Kummerow, C.D., Kojima, M., Oki, R., Nakamura, K., Iguchi, T., 2014. The global precipitation measurement mission. Bull. Am. Meteorol. Soc. 95 (5), 701–722.

Hu, H., Hasekamp, O., Butz, A., Galli, A., Landgraf, J., Aan de Brugh, J., Borsdorff, T., Scheepmaker, R., Aben, I., 2016. The operational methane retrieval algorithm for TROPOMI. Atmos. Meas. Tech. 9 (11), 5423–5440.

Huntzinger, D., Schwalm, C., Michalak, A., Schaefer, K., King, A., Wei, Y., Jacobson, A., Liu, S., Cook, R., Post, W., et al., 2013. The North American carbon program multi-scale synthesis and terrestrial model intercomparison project-part 1: overview and experimental design. Geosci. Model Dev. 6 (6), 2121–2133.

Junk, W.J., de Cunha, C.N., 2005. Pantanal: a large South American wetland at a crossroads. Ecol. Eng. 24 (4), 391–401 Wetland creation.

Kirschke, S., Bousquet, P., Ciais, P., Saunois, M., Canadell, J.G., Dlugokencky, E.J., Bergamaschi, P., Bergmann, D., Blake, D.R., Bruhwiler, L., et al., 2013. Three decades of global methane sources and sinks. Nat. Geosci. 6 (10), 813–823.

Landerer, F.W., Swenson, S.C., 2012. Accuracy of scaled GRACE terrestrial water storage estimates. Water Resour. Res. 48 (4) W04531.

Lehner, B., Döll, P., 2004. Development and validation of a global database of lakes, reservoirs and wetlands. J. Hydrol. 296 (1), 1–22.

Marchetti, Z., Latrubesse, E., Pereira, M., Ramonell, C., 2013. Vegetation and its relationship with geomorphologic units in the Parana River floodplain, Argentina. J. S. Am. Earth Sci. 46 (Supplement C), 122–136.

Marthews, T., Dadson, S., Lehner, B., Abele, S., Gedney, N., 2015. High-resolution global topographic index values for use in large-scale hydrological modelling. Hydrol. Earth Syst. Sci. 19 (1), 91–104.

McNorton, J., Chipperfield, M.P., Gloor, M., Wilson, C., Feng, W., Hayman, G.D., Rigby, M., Krummel, P.B., O'Doherty, S., Prinn, R.G., Weiss, R.F., Young, D., Dlugokencky, E., Montzka, S.A., 2016a. Role of OH variability in the stalling of the global atmospheric CH4 growth rate from 1999 to 2006. Atmos. Chem. Phys. 16 (12), 7943–7956.

McNorton, J., Gloor, E., Wilson, C., Hayman, G.D., Gedney, N., Comyn-Platt, E., Marthews, T., Parker, R.J., Boesch, H., Chipperfield, M.P., 2016b. Role of regional wetland emissions in atmospheric methane variability. Geophys. Res. Lett. 43 (21), 11,433–11,444 2016GL070649.

Melton, J., Wania, R., Hodson, E., Poulter, B., Ringeval, B., Spahni, R., Bohn, T., Avis, C., Beerling, D., Chen, G., et al., 2013. Present state of global wetland extent and wetland methane modelling: conclusions from a model intercomparison project (WETCHIMP). Biogeosciences 10, 753–788.

Myhre, G., Shindell, D., Bréon, F.-M., Collins, W., Fuglestvedt, J., Huang, J., Koch, D., Lamarque, J.-F., Lee, D., Mendoza, B., Nakajima, T., Robock, A., Stephens, G., Takemura, T., Zhang, H., 2013. Anthropogenic and natural radiative forcing. In: Stocker, T., Qin, D., Plattner, G.-K., Tignor, M., Allen, S., Boschung, J., Nauels, A., Xia, Y., Bex, V., Midgley, P. (Eds.), Climate Change 2013: The Physical Science Basis. Contribution of Working Group I to the Fifth Assessment Report of the Intergovernmental Panel on Climate Change. Cambridge University Press, pp. 659–740 Ch. 8.

Nisbet, E., Dlugokencky, E., Bousquet, P., 2014. Methane on the rise - again. Science 343 (6170), 493–495.

Nisbet, E., Dlugokencky, E., Manning, M., Lowry, D., Fisher, R., France, J., Michel, S., Miller, J., White, J., Vaughn, B., et al., 2016. Rising atmospheric methane: 2007–2014 growth and isotopic shift. Glob. Biogeochem. Cycles 30 (9), 1356–1370.

NOAA, 2017. Curve Fitting Methods Applied to Time Series in NOAA/ESRL/GMD. https://www.esrl.noaa.gov/gmd/ccgg/mbl/crvfit/crvfit.html.

O'Dell, C.W., Connor, B., Bösch, H., O'Brien, D., Frankenberg, C., Castano, R., Christi, M., Eldering, D., Fisher, B., Gunson, M., McDuffie, J., Miller, C.E., Natraj, V., Oyafuso, F., Polonsky, I., Smyth, M., Taylor, T., Toon, G.C., Wennberg, P.O., Wunch, D., 2012. The ACOS CO2 retrieval algorithm-Part 1: description and validation against synthetic observations. Atmos. Meas. Tech. 5 (1), 99–121.

Olivier, J., Janssens-Maenhout, G., Peters, J., 2012. Trends in Global CO2 Emissions 2012 Report. PBL Netherlands Environmental Assessment Agency, Hague, Neth.

Pangala, S.R., Enrich-Prast, A., Basso, L.S., Peixoto, R.B., Bastviken, D., Hornibrook, E.R.C., Gatti, L.V., Marotta, H., Calazans, L.S.B., Sakuragui, C.M., Bastos, W.R., Malm, O., Gloor, E., Miller, J.B., Gauci, V., 2017. Large emissions from floodplain trees close the Amazon methane budget. Nature 552, 230 12.

Parker, R., Boesch, H., Cogan, A., Fraser, A., Feng, L., Palmer, P.I., Messerschmidt, J., Deutscher, N., Griffith, D.W.T., Notholt, J., Wennberg, P.O., Wunch, D., 2011. Methane observations from the Greenhouse Gases Observing SATellite: comparison to ground-based TCCON data and model calculations. Geophys. Res. Lett. 38 (15).

Parker, R.J., Boesch, H., Byckling, K., Webb, A.J., Palmer, P.I., Feng, L., Bergamaschi, P., Chevallier, F., Notholt, J., Deutscher, N., Warneke, T., Hase, F., Sussmann, R., Kawakami, S., Kivi, R., Griffith, D.W.T., Velazco, V., 2015. Assessing 5 years of GOSAT proxy XCH4 data and associated uncertainties. Atmos. Meas. Tech. 8 (11), 4785–4801.

Pasquini, A.I., Depetris, P.J., 2007. Discharge trends and flow dynamics of South American rivers draining the southern Atlantic seaboard: an overview. J. Hydrol. 333 (2), 385–399.

Pasquini, A.I., Depetris, P.J., 2010. ENSO-triggered exceptional flooding in the Parana River: where is the excess water coming from? J. Hydrol. 383 (3), 186–193.

Patra, P.K., Houweling, S., Krol, M., Bousquet, P., Belikov, D., Bergmann, D., Bian, H., Cameron-Smith, P., Chipperfield, M.P., Corbin, K., Fortems-Cheiney, A., Fraser, A., Gloor, E., Hess, P., Ito, A., Kawa, S.R., Law, R.M., Loh, Z., Maksyutov, S., Meng, L., Palmer, P.I., Prinn, R.G., Rigby, M., Saito, R., Wilson, C., 2011. TransCom model simulations of CH_4 and related species: linking transport, surface flux and chemical loss with CH_4 variability in the troposphere and lower stratosphere. Atmos. Chem. Phys. 11 (24), 12813–12837.

Patra, P.K., Takigawa, M., Ishijima, K., Cunnold, D., Dlugokencky, E.J., Fraser, P., Gomez-Pelaez, A.J., Tae-Young, G., Jeong-Sik, K., Krummel, P., et al., 2009. Growth rate, seasonal, synoptic, diurnal variations and budget of methane in the lower atmosphere. J. Meteorol. Soc. Jpn. Ser. II 87 (4), 635–663.

Polonsky, I.N., O'Brien, D.M., Kumer, J.B., O'Dell, C.W., the geoCARB Team, 2014. Performance of a geostationary mission, geoCARB, to measure CO_2, CH_4 and CO column-averaged concentrations. Atmos. Meas. Tech. 7 (4), 959–981.

Puig, A., Olguín Salinas, H.F., Borús, J.A., 2016. Relevance of the Paraná River hydrology on the fluvial water quality of the delta biosphere reserve. Environ. Sci. Pollut. Res. 23 (12), 11430–11447 Jun.

Quegan, S., Chave, J., Dall, J., Le Toan, T., Papathanassiou, K., Rocca, F., Saatchi, S., Scipal, K., Shugart, H., Ulander, L., Williams, M., 2012. The Science and Measurement Concepts Underlying the BIOMASS Mission. IEEE, pp. 5542–5545.

Randerson, J., Van Der Werf, G., Giglio, L., Collatz, G.J., Kasibhatla, P.S., 2015. Global Fire Emissions Database, Version 4, (GFEDv4).

Rigby, M., Montzka, S.A., Prinn, R.G., White, J.W.C., Young, D., O'Doherty, S., Lunt, M.F., Ganesan, A.L., Manning, A.J., Simmonds, P.G., Salameh, P.K., Harth, C.M., Mühle, J., Weiss, R.F., Fraser, P., Steele, L.P., Krummel, P.B., McCulloch, A., Park, S., 2017. Role of atmospheric oxidation in recent methane growth. Proc. Natl. Acad. Sci. 114 (21), 5373–5377.

Rigby, M., Prinn, R.G., Fraser, P.J., Simmonds, P.G., Langenfelds, R.L., Huang, J., Cunnold, D.M., Steele, L.P., Krummel, P.B., Weiss, R.F., O'Doherty, S., Salameh, P.K., Wang, H.J., Harth, C.M., Muhle, J., Porter, L.W., 2008. Renewed growth of atmospheric methane. Geophys. Res. Lett. 35 (22).

Riley, W.J., Subin, Z.M., Lawrence, D.M., Swenson, S.C., Torn, M.S., Meng, L., Mahowald, N.M., Hess, P., 2011. Barriers to predicting changes in global terrestrial methane fluxes: analyses using CLM4Me, a methane biogeochemistry model integrated in CESM. Biogeosciences 8 (7), 1925–1953.

Ringeval, B., de Noblet-Ducoudré, N., Ciais, P., Bousquet, P., Prigent, C., Papa, F., Rossow, W.B., 2010. An attempt to quantify the impact of changes in wetland extent on methane emissions on the seasonal and interannual time scales. Glob. Biogeochem. Cycles 24 (2) GB2003.

Saunois, M., Bousquet, P., Poulter, B., Peregon, A., Ciais, P., Canadell, J.G., Dlugokencky, E.J., Etiope, G., Bastviken, D., Houweling, S., Janssens-Maenhout, G., Tubiello, F.N., Castaldi, S., Jackson, R.B., Alexe, M., Arora, V.K., Beerling, D.J., Bergamaschi, P., Blake, D.R., Brailsford, G., Brovkin, V., Bruhwiler, L., Crevoisier, C., Crill, P., Covey, K., Curry, C., Frankenberg, C., Gedney, N., Höglund-Isaksson, L., Ishizawa, M., Ito, A., Joos, F., Kim, H.-S., Kleinen, T., Krummel, P., Lamarque, J.-F., Langenfelds, R., Locatelli, R., Machida, T., Maksyutov, S., McDonald, K.C., Marshall, J., Melton, J.R., Morino, I., Naik, V., O'Doherty, S., Parmentier, F.-J.W., Patra, P.K., Peng, C., Peng, S., Peters, G.P., Pison, I., Prigent, C., Prinn, R., Ramonet, M., Riley, W.J., Saito, M., Santini, M., Schroeder, R., Simpson, I.J., Spahni, R., Steele, P., Takizawa, A., Thornton, B.F., Tian, H., Tohjima, Y., Viovy, N., Voulgarakis, A., van Weele, M., van der Werf, G.R., Weiss, R., Wiedinmyer, C., Wilton, D.J., Wiltshire, R., Worthy, D., Wunsch, D.B., Xu, X., Yoshida, Y., Zhang, B., Zhang, Z., Zhu, Q., 2016. The global methane budget 2000–2012. Earth Syst. Sci. Data 8 (2), 697–751.

Schaefer, H., Fletcher, S.E.M., Veidt, C., Lassey, K.R., Brailsford, G.W., Bromley, T.M., Dlugokencky, E.J., Michel, S.E., Miller, J.B., Levin, I., Lowe, D.C., Martin, R.J., Vaughn, B.H., White, J.W.C., 2016. A 21st-century shift from fossil-fuel to biogenic methane emissions indicated by 13CH4. Science 352 (6281), 80–84.

Schroeder, R., McDonald, K.C., Chapman, B.D., Jensen, K., Podest, E., Tessler, Z.D., Bohn, T.J., Zimmermann, R., 2015. Development and evaluation of a multi-year fractional surface water data set derived from active/passive microwave remote sensing data. Remote Sens. 7 (12), 16688–16732.

Sivapalan, M., Beven, K., Wood, E.F., 1987. On hydrologic similarity: 2. A scaled model of storm runoff production. Water Resour. Res. 23 (12), 2266–2278.

Thoning, K.W., Tans, P.P., Komhyr, W.D., 1989. Atmospheric carbon dioxide at Mauna Loa Observatory: 2. analysis of the NOAA GMCC data, 1974–1985. J. Geophys. Res.: Atmos. 94 (D6), 8549–8565.

Turner, A.J., Frankenberg, C., Wennberg, P.O., Jacob, D.J., 2017. Ambiguity in the causes for decadal trends in atmospheric methane and hydroxyl. Proc. Natl. Acad. Sci. 114 (21), 5367–5372.

Turner, A.J., Jacob, D.J., Wecht, K.J., Maasakkers, J.D., Lundgren, E., Andrews, A.E., Biraud, S.C., Boesch, H., Bowman, K.W., Deutscher, N.M., Dubey, M.K., Griffith, D.W.T., Hase, F., Kuze, A., Notholt, J., Ohyama, H., Parker, R., Payne, V.H., Sussmann, R., Sweeney, C., Velazco, V.A., Warneke, T., Wennberg, P.O., Wunch, D., 2015. Estimating global and North American methane emissions with high spatial resolution using GOSAT satellite data. Atmos. Chem. Phys. 15 (12), 7049–7069.

Walters, D., Best, M., Bushell, A., Copsey, D., Edwards, J., Falloon, P., Harris, C., Lock, A., Manners, J., Morcrette, C., et al., 2011. The Met office unified model global atmosphere 3.0/3.1 and JULES global land 3.0/3.1 configurations. Geosci. Model Dev. 4 (4), 919.

Webb, A.J., Bösch, H., Parker, R.J., Gatti, L.V., Gloor, E., Palmer, P.I., Basso, L.S., Chipperfield, M.P., Correia, C.S.C., Domingues, L.G., Feng, L., Gonzi, S., Miller, J.B., Warneke, T., Wilson, C., 2016. CH4 concentrations over the Amazon from GOSAT consistent with in situ vertical profile data. J. Geophys. Res.: Atmos. 121 (18), 11,006–11,020 2016JD025263.

Wecht, K., Jacob, D., Sulprizio, M., Santoni, G., Wofsy, S., Parker, R., Bösch, H., Worden, J., 2014. Spatially resolving methane emissions in California: constraints from the CalNex aircraft campaign and from present (GOSAT, TES) and future (TROPOMI, geostationary) satellite observations. Atmos. Chem. Phys. Discuss. 14 (3), 4119–4148.

Wennberg, P.O., Roehl, C., Wunch, D., Toon, G.C., Blavier, J.-F., Washenfelder, R., Keppel-Aleks, G., Allen, N., Ayers, J., 2014a. TCCON Data From Park Falls (US), Release GGG2014R0. TCCON data archive, hosted by CaltechDATA.

Wennberg, P.O., Wunch, D., Roehl, C., Blavier, J.-F., Toon, G.C., Allen, N., Dowell, P., Teske, K., Martin, C., Martin, J., 2014. TCCON Data from Lamont (US), Release GGG2014R0. TCCON data archive, hosted by CaltechDATA.

Wilson, C., Chipperfield, M.P., Gloor, M., Chevallier, F., 2014. Development of a Variational Flux Inversion System (INVICAT v1.0) Using the TOMCAT Chemical Transport Model. Geosci. Model Dev. 7 (5), 2485–2500.

Wunch, D., Toon, G.C., Blavier, J.-F. L., Washenfelder, R.A., Notholt, J., Connor, B.J., Griffith, D.W.T., Sherlock, V., Wennberg, P.O., 2011a. The total carbon column observing network. Philos. Trans. R. Soc. Lond. A Math. Phys. Eng. Sci. 369 (1943), 2087–2112.

Wunch, D., Toon, G.C., Wennberg, P.O., Wofsy, S.C., Stephens, B.B., Fischer, M.L., Uchino, O., Abshire, J.B., Bernath, P., Biraud, S.C., Blavier, J.-F. L., Boone, C., Bowman, K.P., Browell, E.V., Campos, T., Connor, B.J., Daube, B.C., Deutscher, N.M., Diao, M., Elkins, J.W., Gerbig, C., Gottlieb, E., Griffith, D.W.T., Hurst, D.F., Jiménez, R., Keppel-Aleks, G., Kort, E.A., Macatangay, R., Machida, T., Matsueda, H., Moore, F., Morino, I., Park, S., Robinson, J., Roehl, C.M., Sawa, Y., Sherlock, V., Sweeney, C., Tanaka, T., Zondlo, M.A., 2010. Calibration of the total carbon column observing network using aircraft profile data. Atmos. Meas. Tech. 3 (5), 1351–1362.

Wunch, D., Wennberg, P.O., Toon, G.C., Connor, B.J., Fisher, B., Osterman, G.B., Frankenberg, C., Mandrake, L., O'Dell, C., Ahonen, P., Biraud, S.C., Castano, R., Cressie, N., Crisp, D., Deutscher, N.M., Eldering, A., Fisher, M.L., Griffith, D.W.T., Gunson, M., Heikkinen, P., Keppel-Aleks, G., Kyrö, E., Lindenmaier, R., Macatangay, R., Mendonca, J., Messerschmidt, J., Miller, C.E., Morino, I., Notholt, J., Oyafuso, F.A., Rettinger, M., Robinson, J., Roehl, C.M., Salawitch, R.J., Sherlock, V., Strong, K., Sussmann, R., Tanaka, T., Thompson, D.R., Uchino, O., Warneke, T., Wofsy, S.C., 2011b. A method for evaluating bias in global measurements of CO_2 total columns from space. Atmos. Chem. Phys. 11 (23), 12317–12337.

Yan, X., Akiyama, H., Yagi, K., Akimoto, H., 2009. Global estimations of the inventory and mitigation potential of methane emissions from rice cultivation conducted using the 2006 intergovernmental panel on climate change guidelines. Glob. Biogeochem. Cycles 23 (2) GB2002.

Zhu, Q., Peng, C., Ciais, P., Jiang, H., Liu, J., Bousquet, P., Li, S., Chang, J., Fang, X., Zhou, X., Chen, H., Liu, S., Lin, G., Gong, P., Wang, M., Wang, H., Xiang, W., Chen, J., 2017. Interannual variation in methane emissions from tropical wetlands triggered by repeated el niño southern oscillation. Glob. Chang. Biol. 23 (11), 4706–4716.